# 3-D hydromechanical simulation of intersecting faults: Influences on fluid circulation and formation of oriented-orebodies

Khalifa Eldursi, Luc Scholtes, Marianne Conin, Fabrice Golfier, Patrick Ledru, Julien Mercadier, Pauline Collon, Remy Chemillac

# 3-D hydromechanical simulation of intersecting faults: Influences on fluid circulation and formation of oriented-orebodies

Khalifa ELDURSI[a,b,*], Luc SCHOLTES[b,c], Marianne CONIN[b], Fabrice GOLFIER[b], Patrick LEDRU[b], Julien MERCADIER[b], Pauline COLLON[b], Remy CHEMILLAC[d]

[a] Department of Earth Sciences, University of Benghazi, PO BOX 9480-1308, Benghazi, Libya

[b] Université de Lorraine, CNRS, GeoRessources, 54000 Nancy, France

[c] Université Clermont Auvergne, CNRS, IRD, OPGC, Laboratoire Magmas et Volcans, Clermont-Ferrand, France

[d] Orano Canada, 100-833 45th Street West, Saskatoon, Saskatchewan S7L 5X2 , Canada

[*] Corresponding author
Phone: +218918824824
E-mail: khalifa.eldursi@gmail.com

Keywords: fault intersection; fault activation; structurally-controlled mineral deposits; 3-D hydromechanical modeling; uranium deposits; Athabasca Basin

**Abstract**

Although intersection zones of two or more fault arrays have been identified as favorable loci of unconformity-related basin-basement mineral deposits in previous studies, their roles in controlling fluid flow patterns related to formation of oriented-, and structurally-controlled mineral deposits remain unclear. In this study, 3-D hydromechanical models were conducted to better understand the response of a natural fault intersected by a hydraulic fault under different stress regimes. A comprehensive parametric study was carried out to assess the roles of fluid pressure, burial depth, basin permeability, intersection angle, and horizontal differential stress on the hydromechanical response of a system containing two intersecting faults. Depending on basin sediment permeability, fault intersection angle, and horizontal differential stress, the fluid flow either stops, crosses, or diverts toward natural fault. Among the tested parameters, the intersection angle, and horizontal differential stress have the most noticeable effect on the fluid flow in the system. The critical intersection angle at which the fluid flow diverts toward the natural fault varies between $\approx 27^{\circ}$ in normal faulting regimes, to $\approx 55^{\circ}$, in both strike-slip and reverse faulting regimes. Conversely, burial depth and fluid pressure have no significant effect on fluid flow diversion in the intersection zone. The results are in agreement with field observations related to the unconformity-related uranium deposits found in northern Canada.

## 1. Introduction

Unconformity-related basement/basin metallic mineral deposits such as Mississippi Valley-type (MVT), SEDimentary EXhalative (SEDEX), and Unconformity-Related Uranium (URU) deposits (also containing associated metals, such as As, Ni, Au, Pb, As, V, REEs, Mo, and Te) are considered to be the largest economic sources of major commodity metal(s). Although these deposits are different in terms of tectonic settings, formation mechanisms, and/or ages, they are all defined as structurally-controlled mineral deposits and display some common elements (Hoeve and Quirt, 1984, Leach et al., 2001; Muchez et al., 2005; Shepherd et al., 2005; Jefferson et al., 2007; Wilkinson 2014; Emsbo et al., 2016 and references therein).

In such systems, the flow of one or more fluids have been implicated in the formation of mineralization through fluid-rock or fluid-fluid (fluid mixing) interactions (e.g., Hoeve and Quirt, 1984; Leach et al., 2001; Jefferson et al., 2007; Wilkinson, 2014). However, despite the fact that chemical reactions and mass transport are the main processes responsible for the formation of mineral deposits, their actual spatial locations essentially rely on fluid flow patterns that, in turn, are strongly influenced by fault systems at both basin and deposit scales. The formation of mineral deposits requires a large amount of fluid to be circulated between the source and depositional sites (e.g., Fayek and Keyser, 1997; Alexandre et al., 2009; Aquilina et al., 2011). In structurally-controlled mineral deposits, faults and associated fractures (damage zone) are advocated as being favorable fluid pathways particularly in intrinsically low-permeability environments (Polito et al., 2004; Huston et al., 2010). Therefore, the circulation of fluids through activated fault zones remains of broad interest to a variety of different mineral commodities (e.g., Sibson, 1995; Kyser et al., 2000; Ford et al., 2009; Cui et al., 2012; Power et al., 2012; Wilkinson, 2014; Emsbo et al., 2016; Li et al., 2018; Eldursi et al., 2021a).

During the last two decades, numerous numerical studies have been carried out to improve our understanding of the effects of fault geometries (e.g., fault dip, width, bend/jog angle, length, spacing and interconnection/intersections, mechanical properties, deformation rates, and host lithologies) on fluid flow patterns and formation of mineral deposits (e.g., Cui et al., 2012; Person et al., 2012; Li et al., 2018; Eldursi et al., 2021a and references therein). Among the aforementioned structural characteristics, and based on field studies and observations, fault intersections emerge as a strong structural attribute in the control of fluid flow patterns and therefore the loci of mineral deposits (Jefferson et al., 2007; Ford et al., 2009; Person et al., 2012; Huston et al., 2016). In the following, the term “intersection angle” designates the angular difference in strike between two intersecting fault planes and the term “intersection zone” defines the spatial location of their cross-cutting intersection (Peacock et al., 2016).

Nonetheless, the role of intersection zones on fluid circulations and their effects on mineralization geometries is unclear. For instance, the uranium deposits in the Athabasca Basin, Canada show a good correlation between fault intersections and locations of the deposits (e.g., Jefferson et al., 2007). In the eastern part of the basin, the deposits are aligned along NE regional deep-seated shear zones that are related to the Wollaston-Mudjatik Transition Zone at the regional scale (Fig. 1). However, U deposits demonstrate a change in orientation at the local scale (e.g.; Cigar Lake,

Collins Bay, Key Lake, Millenium, and Sue deposits) or a deviation in their spatial distribution due to intersection zones of two or more superficial and local fault arrays that are not shown in figure 1 (e.g., J Zone (Fig. 1A #3), McClean North (Fig. 1A #4), Collins Bay (Fig. 1A #7), Midwest (Fig. 1A #10), Christie Lake (Fig. 1A #11), and Phoenix (Fig. 1A #12)). Therefore, the intersection zone may deviate locally the stress state, leading to impede or facilitate the activation of an intersecting fault. Thus, numerical approach may be required to better understand mechanisms that govern fluid flow at intersection zones.

Furthermore, the fault-valve model was introduced by Sibson et al. (1988), Cox (1991), Cox et al. (2001), Cox and Ruming (2004), Cox (2005), and Pochon et al. (2018) among others, to explain the role of fault systems in transfer fluids from deeper crustal levels to shallower portions. Their studies highlighted the role of fault intersection as potential sites for governing and localizing fluid flow, and the formation of different mineral deposits (e.g., Ag, Zn-Pb-Ag, Fe-Cu-Pb-Zn, Sb-Au deposits). This model describes how deep basement fluids under supra-lithostatic regime can be discharged toward the upper crust. According to Sibson, (1996), Vidale and Shearer (2006), Shelly et al. (2014), and Ruhl et al. (2016), the injected fluid triggers faulting and provides a potential reactivation mechanism of preexisting fault systems. For what concerns the Athabasca Basin, previous works (e.g., Kotzer and Kyser, 1995; Jefferson et al., 2007; Chi et al., 2019) discussed the potential role of deep-seated regional faults as fault-valves to move and discharge deep basement fluids as an addition to the diagenetic-hydrothermal basement-sandstone fluid-fluid and/or fluid-rock interaction genetic model originally presented by Hoeve and Sibbald (1978), Hoeve and Quirt (1984), and Wallis et al. (1985). However, the studies did not explain how such a mechanism induces fault reactivation and formation of oriented ore deposits in the shallow crustal portion.

The present study discusses: 1) the reactivation mechanisms of a two-fault system in response to hydromechanical processes at fault intersections; 2) the role of the intersection angle and faulting regimes (normal, reverse, and strike-slip faulting regimes, as described by Anderson's model, 1951) on the response of the fault system and on the fluid flow pattern (crosses, diverts or stops at the intersection); 3) the implication of the numerical results for the formation of oriented mineral deposits, in terms of their genesis and exploration.

Although previous numerical studies have evaluated fault activation and permeability evolution due to fluid propagation using a similar discrete element approach (e.g., Pascal, 2002; Derode et al., 2015; Guglielmi et al., 2015; Huang et al., 2016; Cappa et al., 2018; Kakurina et al., 2019; Shiu et al., 2021), the present study is novel compared to previously-published studies as: 1) the boundary and initial conditions are constrained by field measurements and observations; 2) two layers (sedimentary basin and crystalline basement lithologies) of different permeabilities are considered, with fluid exchange between the layers and faults being allowed; 3) the models are applied at the scale of a mineral deposit; and 4) the study provides an explicit link between fault activation and formation of oriented mineral deposits.

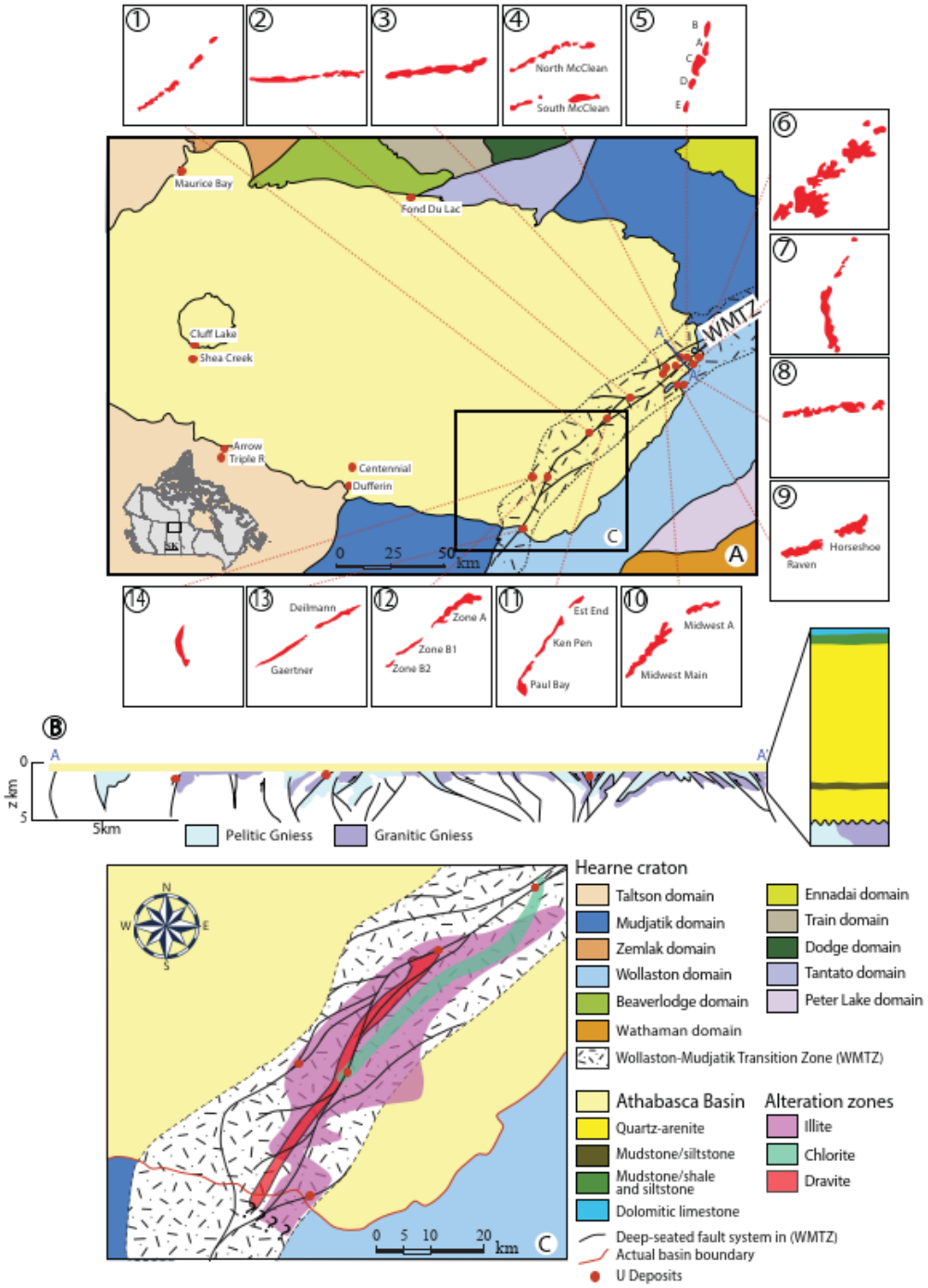


Fig. 1 A) Major structural and geological features, and discovered uranium deposits in the Athabasca basin; B) simplified cross and columnar sections show general basement and basin units; C) map of alteration patterns (illite, chlorite, and dravite) of the southeastern part of the Athabasca Basin; (modified after Earle and Sopuck 1989). (1) McArthur deposit, Dee Guffey (2017); (2) Cigar Lake deposit, Eldursi et al. (2021); (3) J Zone deposit, Graham (2020); (4) McClean deposit, Tremblay (1982); (5) Sue deposit, Li et al. (2018); (6) Eagle Point deposit, IAEA (2018); (7) Collins Bay deposit, IAEA (2018); (8) Roughrider deposit, Boulanger (2012); (9) Raven and Horseshoe deposit, Rhys et al. (2010); (10) Midwest deposit; Benedicto, (2018); (11) Christie deposit; Perkins et al. (2017); (12) Phoenix deposit, Power et al. (2012); (13) Key Lake deposit, Dahlkamp (1978); (14) Millennium deposit, Cloutier et al (2009). The deposits are not to scale; the question marks indicate the unknown source of fluid.

## 2. Geological setting of the Athabasca Basin and its uranium deposits

Uranium deposits in the Athabasca Basin, northern Saskatchewan (Canada) are well known for their high-grade and large-tonnage reserves (IAEA, 2018). They have therefore been subjected of numerous and intensive studies of different kinds (e.g., economic geological, mineralogical, geochemical, structural, sedimentological, numerical) that have provided large field data and measurements (e.g., mineralization geometries, fault networks, physical parameters, metallogenetic models). Because of this, they have been used in this study as type example for unconformity-related basin-basement interaction mineral deposits. The Athabasca Basin comprises late Paleoproterozoic to Mesoproterozoic quartz arenite, with minor conglomerate and siltstone. Some stromatolitic carbonate, mudstone, shale, and siltstone occur at the top of the preserved sedimentary pile. The basin unconformably overlies Archean to Paleoproterozoic igneous and high-grade metamorphic rocks (granitic orthogneisses, felsic to mafic intrusive rocks, and metasedimentary paragneisses; ((Fig. 1B); for more details see Annesley et al., 2005; Jefferson et al., 2007; Card et al., 2018; Ledru et al., 2019; Poh et al., 2020, 2022; Ledru et al., 2023 and references therein). The URU deposits hosted by the Athabasca Basin and the underlying basement lithologies are classified as epigenetic unconformity-related, and structurally-controlled mineral deposits due to their proximity to the sub-Athabasca unconformity surface, and spatial correlation to fault systems. Furthermore, the fault systems in the Athabasca Basin are classified into two categories: 1) regional deep-seated shear zones (Fig. 1); and 2) superficial local reverse and strike-slip faults (e.g., Hoeve and Sibbald 1978; Dahlkamp 1978; Tremblay 1982; Hoeve and Quirt 1984; Quirt 2003; Eldursi et al. 2021a; Poh et al. 2022) which are not shown in figure 1. However, the tectonic evolution of the deep-seated shear zones is still in debate (for more details see Annesley et al. 2005; Card et al. 2007; Jeanneret et al. 2016; Ledru et al. 2019; Poh et al. 2020; Eldursi et al. 2021b; Poh et al. 2022; Ledru et al. 2023). Although the majority of discovered URU deposits are located mainly in the eastern part of the basin, within and along these regional deep-seated shear systems that are located within the Wollaston-Mudjatik Transitional Zone (WMTZ; Fig. 1A), their geometries and spatial distribution are controlled by intersected local and superficial fault arrays (e.g., Eldursi et al. 2021a)..

The intersection zones of two or more arrays of these superficial faults are associated with breccia zones, and are within clay mineral, hematization/bleaching, and silicification/desilicification host-rock alteration haloes. Unconformity (sandstone) mineralization can be found up to 40 m above and/or below the unconformity, while basement-hosted mineralization can occur up to several hundred metres below the unconformity (Hoeve and Quirt, 1984; Quirt, 2003; Jefferson et al., 2007).

The diagenetic-hydrothermal basement-sandstone interaction metallogenetic model for the URU uranium mineralization (Hoeve and Sibbald, 1978; Hoeve and Quirt, 1984, Wallis et al., 1985) describes basement-sandstone fluid interactions and redox-controlled U mineralization that occurred near the sub-Athabasca unconformity. This model suggests that the deposits formed under reducing conditions near the unconformity through interaction between oxidizing basinal fluids and a reducing basement fluid and/or reduced basement lithologies (Hoeve and Sibbald,

1978; Hoeve and Quirt, 1984; Wallis et al., 1985; Wilson and Kyser, 1987; Kotzer and Kyser, 1995; Fayek and Kyser, 1997; Quirt ,2003; Jefferson et al., 2007; among others). Further studies on the URU metallogenesis by Cloutier et al. (2009), Rhys et al. (2010), Boulanger (2012), Perkins et al. (2017), Benedicto (2018) IAEA (2018), Li et al. (2018), Li et al. (2021), Guffey, et al. (2019), Graham (2020), and Eldursi et al. (2021a), among others, have provided more details on the fluid sources and the fluid flow regimes. Interaction of such fluids with each other (fluid-fluid interaction at the unconformity) and of basinal fluid with basement lithologies and fluids (fluid-rock and fluid-fluid interactions occurring below the unconformity) resulted in precipitation of uranium and other metals (Quirt, 2003).

The URU mineralization, as noted above, is also sub-classified according to its location relative to the unconformity surface to: 1) polymetallic basin-hosted uranium deposits that ride the unconformity and extend into the basin along cataclastic breccia and fracture zones (the egress-style mineralization; e.g., Cigar Lake, Collins Bay, Fox Lake, Midwest deposits), and 2) monometallic, breccia- and vein-associated basement-hosted deposits (ingress-style mineralization, e.g., Rabbit Eagle Point, Arrow, Millennium deposits). Several deposits show both sub-classes of mineralization (e.g., McArthur River, Key Lake, Shea Creek). Disregarding the mechanisms through which the uranium deposits were formed (Kyser et al., 2000; Cuney, 2009), the metallogenetic model advocates fluid circulation through fault arrays at regional and local scales as an agent to dissolve, carry, and precipitate metals. Although the sources of the fluids are still a matter of debate, the form and shape of the alteration patterns point out different probable fluid flow episodes and, in the WMTZ, the northeast direction as a preferred fluid pathway at the regional scale. The map of regional alteration patterns of chlorite, dravite, and illite illustrates this northeast trend based on normative clay mineral determinations techniques applied to 6500 core samples from exploration drill holes (Fig. 1C; Earle and Sopuck, 1989).

Thomas et al. (2016) provided a statistical analysis of the geometry of the uranium deposits of the eastern part of the basin. They demonstrate that the majority of mineral deposits typically have elongate forms and that the majority of them (≈65%) are oriented N50–60E, while the others vary between NNW to EW directions. Although detailed knowledge of fault networks is not available for all mineralization sites, several studies have emphasized that the mineralization are found at and along intersection zones between two or more fault arrays (e.g., Card et al., 2007; Jefferson et al., 2007; Li et al., 2018; Eldursi et al., 2021a). Additionally, the associated-faults are characterized by intense and well-developed microfractures and breccia zones, and reactivated in reverse or strike-slip modes (Card et al., 2003; Annesley et al., 2005; Card et al., 2007; Hillacre, 2018; Benedicto et al., 2021). Fayek and Kyser (1997) and Chi et al. (2018) show that, to form a large high-grade uranium deposit of limited volume, a huge amount of fluid is required to be focussed through that region. Accordingly, presence of oriented mineral deposits is used as an indicator of the main fluid flow path at mineralization sites.

Recently, numerical modeling has demonstrated and discussed the potential roles of local structural architectures and basement lithologies in the formation of URU deposits. For instance, Li et al. (2018) discussed the potential effect of variations in basement lithology on dilation

distribution within the rock matrix and, consequently, the formation of the Sue uranium deposits. Eldursi et al. (2021) demonstrated the critical role of local structural architecture (E-W triangle structural corridor formed by "extended-basement faults") on the formation of the Cigar Lake uranium deposit and the potential role of these faults in the formation of the NNE-SSW plunging structure at the Sue deposits. Nevertheless, no study has been carried out to explicitly investigate the role of the hydromechanical process on fluid flow at intersection zones and, consequently, on the formation of URU mineralization.

## 3. Numerical Modeling

### 3.1 Numerical code and theoretical basis

In this study, the 3D Distinct Element Code (3DEC, version 5.2; Itasca 2013) is utilized to simulate 3D hydromechanically-coupled models of fault intersection zones subjected to pressurized fluid flow (e.g., Pascal, 2002; Cappa et al., 2018; Kakurina et al., 2019; Shiu et al., 2021). Discrete Element Models have proven effective in reproducing some observed fractured rock masses and real fault behaviors (Guglielmi et al., 2008; Yin et al., 2020). Rock blocks and faults are simulated as deformable blocks and inter-block contact surfaces, respectively. Each block is simulated as a deformable block based on a finite difference approach. The behavior of rock blocks is linear elastic as defined by Hooke's law, and determined by their Young's modulus ($E$) and Poisson's ratio (υ). The contact surfaces making up the faults are further discretized into sub-contacts. The linear elastic behavior of these sub-contacts that make up the fault surfaces is defined in both the normal and the shear directions as follows:

$$\Delta F_n = -K_n \Delta U_n A_c \quad (1)$$

$$\Delta F_s = -K_s \Delta U_s A_c \quad (2)$$

where $\Delta F_n, \Delta F_s, K_n, K_s, U_n,$ and $U_s$ are the normal and shear force increments (kN), stiffnesses (Pa.m$^{-1}$), and displacement increments (m), respectively, and $A_c$ is the contact area (m$^2$). When $U_n$>0 the fault dilates, as a result of either direct tensile or shear induced loadings, as expected for classical rock joints (Barton et al, 1973).

Contacts can fail either in shear or in tension. The maximum admissible tensile normal force is defined as:

$$T_{max} = -T A_c \quad (3)$$

with T being the tensile strength (Pa). When tensile failure occurs, the contact force is set to zero. The maximum admissible shear force is defined according to a Mohr-Coulomb criterion such as:

$$F^s_{max} = c A_c + F_n \tan \varphi \quad (4)$$

with $c$ the cohesion (Pa) and $\varphi$ its friction angle. When shear failure occurs, contacts can then slide and shear induces dilation is computed as an additional normal force defined as follows:

$$\Delta F_{n,dil} = K_n \Delta U_s \tan \psi \, A_c \quad (5)$$

where ψ is the dilation angle defined as ($\tan \psi = \frac{\Delta U_n}{\Delta U_s}$).

Fluid flow is simulated in both blocks and faults, and exchanges are allowed between faults and blocks. In the blocks, fluid flow is governed by Darcy's law:

$$\vec{q} = -\frac{k}{\mu_f}\left[\nabla P_f + \rho_f g \vec{z}\right] \quad (6)$$

where $\vec{q}$ is the fluid flux (m.s$^{-1}$), k is the permeability (m$^2$), $\mu_f$ is the fluid dynamic viscosity (kg.m$^{-1}$.s$^{-1}$), $\nabla P$ is the gradient of pore pressure (Pa.m$^{-1}$), $\rho_f$ is the fluid density (kg.m$^{-3}$), $g$ is the gravitational acceleration (m.s$^{-2}$), and $\vec{z}$ the downward unit vector. In the faults, fluid flow is governed by the cubic law, where permeability is defined through the hydraulic aperture $a_h$ (Witherspoon et al., 1980):

$$\vec{Q} = \frac{a_h^3}{12\mu_f}\left[\nabla P_f + \rho_f g \vec{z}\right] \quad (7)$$

where $Q$ is the flow rate per unit width (m$^2$.s$^{-1}$), $P_f$ is the fluid pressure (Pa), and $a_h$ is the hydraulic aperture (m) which can be related to the permeability *k* through Darcy's law ($a_h = \sqrt{12k}$).

The models used in this study are hydromechanically-coupled. The effect of pore pressure in the rock blocks is classically expressed through the effective stress concept, as defined in Biot's theory (Biot, 1956):

$$\sigma_n' = \sigma_n - bP_p \quad (8)$$

where $\sigma_n'$ is the effective normal stress (Pa), $\sigma_n$ is the normal stress (Pa), b is Biot coefficient. A similar relation applies to faults (Walsh, 1981)

$$\sigma_n' = \sigma_n - \alpha P_f \quad (9)$$

where $\alpha$ is the effective stress coefficient. However, Terzaghi's approximation (Terzaghi, 1923) is used in both relations (i.e., *b* and $\alpha$ are equal to 1).

In the faults, the coupling between deformation and fluid pressure is established through the pressure diffusion equation:

$$\frac{\delta P_f}{\delta t} = \frac{{a_h}^2 K_f}{12\mu_f} P_f - \frac{K_f}{a_h}\frac{\delta a_h}{\delta t} \quad (10)$$

where the term $\frac{K_f}{a_h}\frac{\delta a_h}{\delta t}$ represents the change of fluid pressure within the fault due to the deformation of both the rock blocks and the fault, and $K_f$ is the fluid bulk modulus (Pa). In the rock blocks, the flow equations are solved using a finite difference scheme. The changes in fluid content are linked to the volumetric strain ($\epsilon$) of the blocks, and the pore pressure ($P_P$), as follows:

$$\frac{\phi}{K_f}\frac{\delta P_p}{\delta t} = \frac{\delta \xi}{\delta t}\frac{\delta \epsilon}{\delta t} \quad (11)$$

where $\xi$ is the variation of fluid volume (fluid content) per unit volume and $\phi$ is the porosity. For more details on the model, please refer to Itasca (2013).

**3.2 Model geometry, boundaries, and initial conditions**

To study the hydromechanical behavior of a two-faults system subjected to overpressured fluid, a 500*500*200 m cubic model is used, centered at x = 0, y = 250, and z = 6000 m (Fig. 2A). As previously mentioned, the basin is mostly composed of quartz arenite, while the basement is composed of Archean to Paleoproterozoic igneous and high-grade metamorphic rocks. For simplification purpose and as the study focuses on the fault architecture impact, the basin and basement are simulated in the model as two homogeneous layers, each 100 m thick. The basement-basin contact which represents the unconformity surface, is located at 6000 m depth (a scenario at 3,000 m depth is also tested; Pagel, 1975; Chi et al., 2018). As the unconformity surface is treated, similarly to the faults, as a contact surface in the code, different physical properties are assigned to it to avoid opening or displacement occurring along it (Table 1), because the chosen model assumption is to focus on the fluid flow along the faults and in the intersection zone. All the models are discretized with tetrahedra of an average size of 10 and 20 m for the basement and basin domains, respectively. The model resolution has been chosen based on two factors; 1) numerical stability and convergence; 2) computing run times. The latter factor relies also on the time-step which is strongly affected by the size of the elements and the physical properties. For this study, we set up the models to contain approximately 180,000 elements.

In all models, two vertical faults are hosted within the basement layer and they cross-cut each other precisely at the centroid of the layer (Fig. 2A). The fault into which the fluid is injected (hereinafter referred to as the 'hydraulic fault') is parallel to the y-axis and thus perpendicular to the x-axis, while the second fault (hereinafter referred to as 'natural fault') is oriented following the intersection angle. Variations of the intersection angle are obtained by changing the strike direction of the natural fault toward the y-axis (Fig. 2B). To study how oriented mineral deposits can be formed through the propagation of overpressured fluids ("fluid-driven failure"; Sibson, 2001), a fluid of water properties (Table 1) is injected from one lateral side of the hydraulic fault (Fig. 2A). The mechanical stresses applied at the model boundaries were chosen to represent respectively normal, reverse, and strike-slip faulting regimes as defined by Anderson (1951); see Table (2). The principal stress directions correspond to the model axis, so that they are applied along the domain boundary surfaces. In all regimes, the vertical stress is equal to $S_V = \gamma * z$, where $\gamma$ is the average unit weight of saturated porous sandstone (20 $kN/m^3$; Mayne et al., 2010), and z is the depth (m). Accordingly, the vertical stress applied to the upper boundary is calculated (Table 2). The horizontal stresses are adjusted depending on the stress regime. For the normal faulting regime, the horizontal stresses were calculated according to $S_H = K_o * S_V$, where $K_o$ is the coefficient of earth pressure, which can be estimated based on the Poisson's ratio ($\upsilon$) of the rock ($K_o = \upsilon / 1-\upsilon$; Jaky, 1944; Budhu, 2010), with $\upsilon = 3E-2G/2(3E+G)$, where E and G are the bulk and shear moduli of the rock, respectively. The ratio between the maximum and minimum stresses (Differential Stress DS; $\sigma_1 - \sigma_3$) is kept constant for all regimes (36 MPa), whereas, the Horizontal Differential Stress (HDS; $\sigma_H - \sigma_h$) varies from 05, 31, to 36 MPa for normal, reverse, and strike-slip faulting regimes, respectively. In all models, $\sigma_h$, $\sigma_H$, and $\sigma_v$ are fixed to be parallel to the x-, y-, and z-axes, respectively ($\sigma_h = \sigma_x$; $\sigma_H = \sigma_y$; $\sigma_v = \sigma_z$; Fig. 2A). Table (2) lists the values of the boundary stresses applied for each regime.

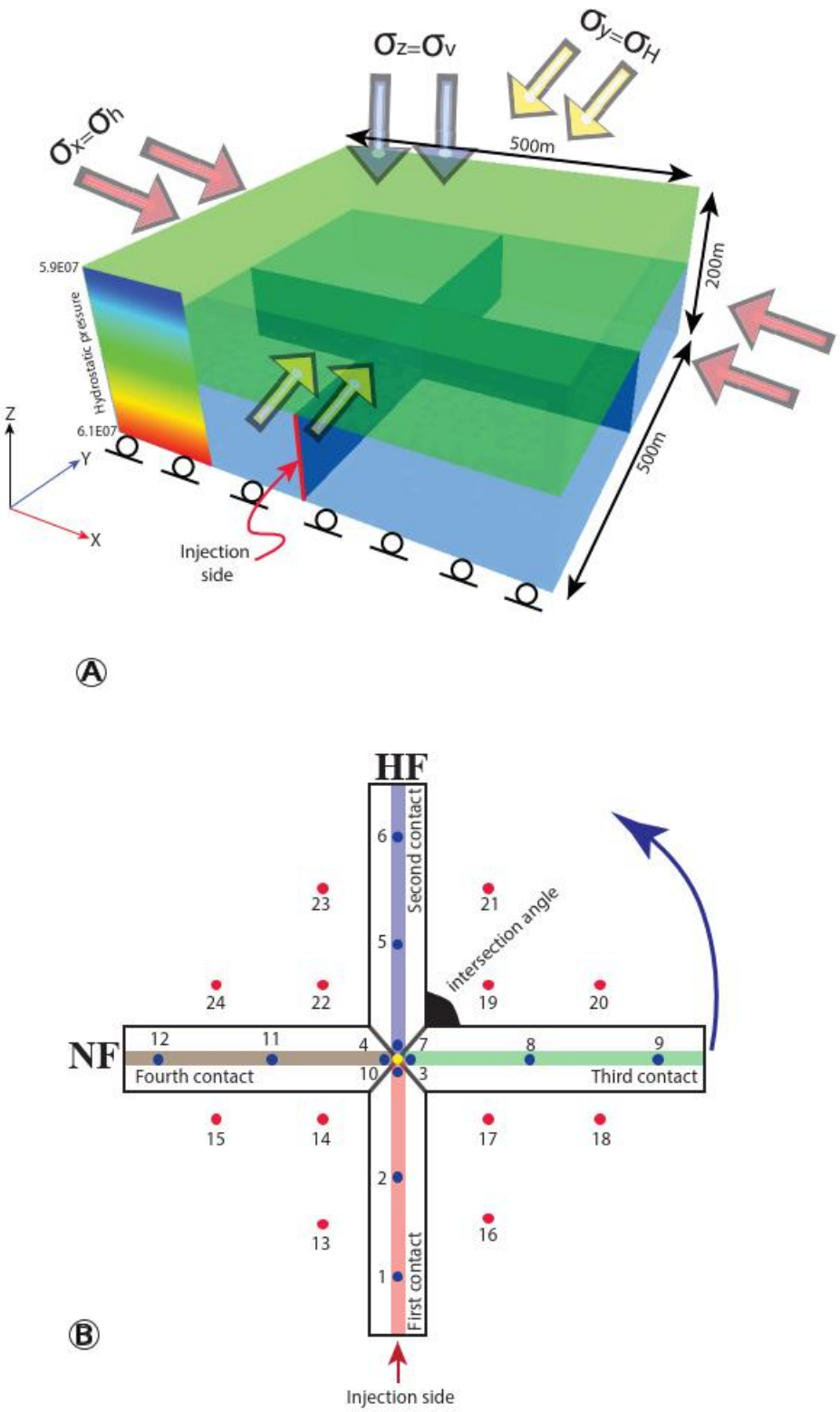


Fig. 2 Numerical modeling protocol: A) dimensions, boundary and initial conditions. Solid red line indicates the place where the over pressured fluid is injected; B) a map view of the two faults system; twenty-five monitoring points (including intersection point "yallow dot") are assigned along the faults (blue dots) and basement layer (red dots). (HF) hydraulic fault, (NF) natural fault.

The pressure value of the injected fluid is defined as a function of the applied stresses for each faulting regime (110% ≥ $P_f$ > 90% of $\sigma_h$ ($\sigma_x$)), consistent with the early stage of post-failure conditions ($P_f > \sigma_1 \sim \sigma_3$) described by Sibson (1995, 2020), where the hydrostatic profile shifts to nearly lithostatic for shallow crustal portions (pore-fluid factor $\lambda_v \approx 1$; Hubbert and Rubey, 1959; Sibson, 2001, 2020). Different values of injection pressure were tested for each regime to assess its influence on the results. However, the results remain similar. In addition, two burial depths are evaluated, respectively equal to 6000, and 3000 m (Pagel, 1975; Chi et al., 2018). The effect of basin permeability is also examined by assigning different permeability values equal to or higher than the initial fault permeability (initial hydraulic aperture $a_0$). Roller-type conditions are defined along the lateral and bottom boundaries of the models, while the upper boundary is kept free to move (Fig. 2A). All boundaries are left open for the fluid to flow (drained conditions).

The numerical simulation comprises three stages: 1) "*mechanical on // fluid off*" to reach the mechanical equilibrium with the predefined vertical and horizontal stresses. Any vertical or horizontal displacement is reset at this stage; 2) "*mechanical off // fluid on*" to apply the hydrostatic fluid pressure once the mechanical equilibrium has been reached. The two previous steps are mandatory for any quasi-static numerical modeling to observe the changes in stress, strain, displacement, fluid flow, and fluid pressure obtained due to a hydro-mechanical perturbation after the initial equilibrium states; 3) the main fully-coupled phase "*mechanical on // fluid on*" where fluid is injected from one side of the hydraulic fault once the hydrostatic pressure field is established. Except for fault permeability, the physical properties for the basement and basin layers, and the faults are constant for all models and regimes (Table 1). In addition, twenty-five recording points are assigned in the models at and around the intersection point either along the faults or in the basement layer to monitor the variation of fluid pressure, normal and shear stresses, and displacements (Fig. 2B). All models are run with equal time-step and total duration.

**3.3 Fault modeling**

Faults at field scale are complex brittle structures, often composed of one or more low-permeability core zone and high-permeability damage zone. Sliding induced deformation mainly localize within the core zone which includes gouge, breccia and cataclasite, whereas subsidiary fractures and minor faults develop within the surrounding damage zone (Fig. 3A; Sibson, 1977; Caine et al., 1996; Berg and Skar, 2005). The fault zone heterogeneity induces a strong spatial permeability variation (Fig. 3B). However, based on the ratio of damage zone to total fault thickness, Caine et al. (1996) classified fault architecture into four end members: distributed conduit; combined conduit-barrier; localized conduit; and localized barrier. Accordingly, the faults in the Athabasca Basin are defined as distributed conduits; and/or combined conduit-barriers as they are characterized by well-developed damage zones (Annesley et al., 2005; Martz et al., 2017, 2019). Furthermore, as the damage zone represents a large area of the fault zone (Fig. 3A; Childs et al., 2009), and for simplification purposes, the fault zones (core and damage zones) are simulated in this study as rock block interfaces with effective mechanical and hydraulic properties (Fig. 3B). The faults' hydromechanical behavior is governed by an elasto-plastic model (see previous section and Table 1).

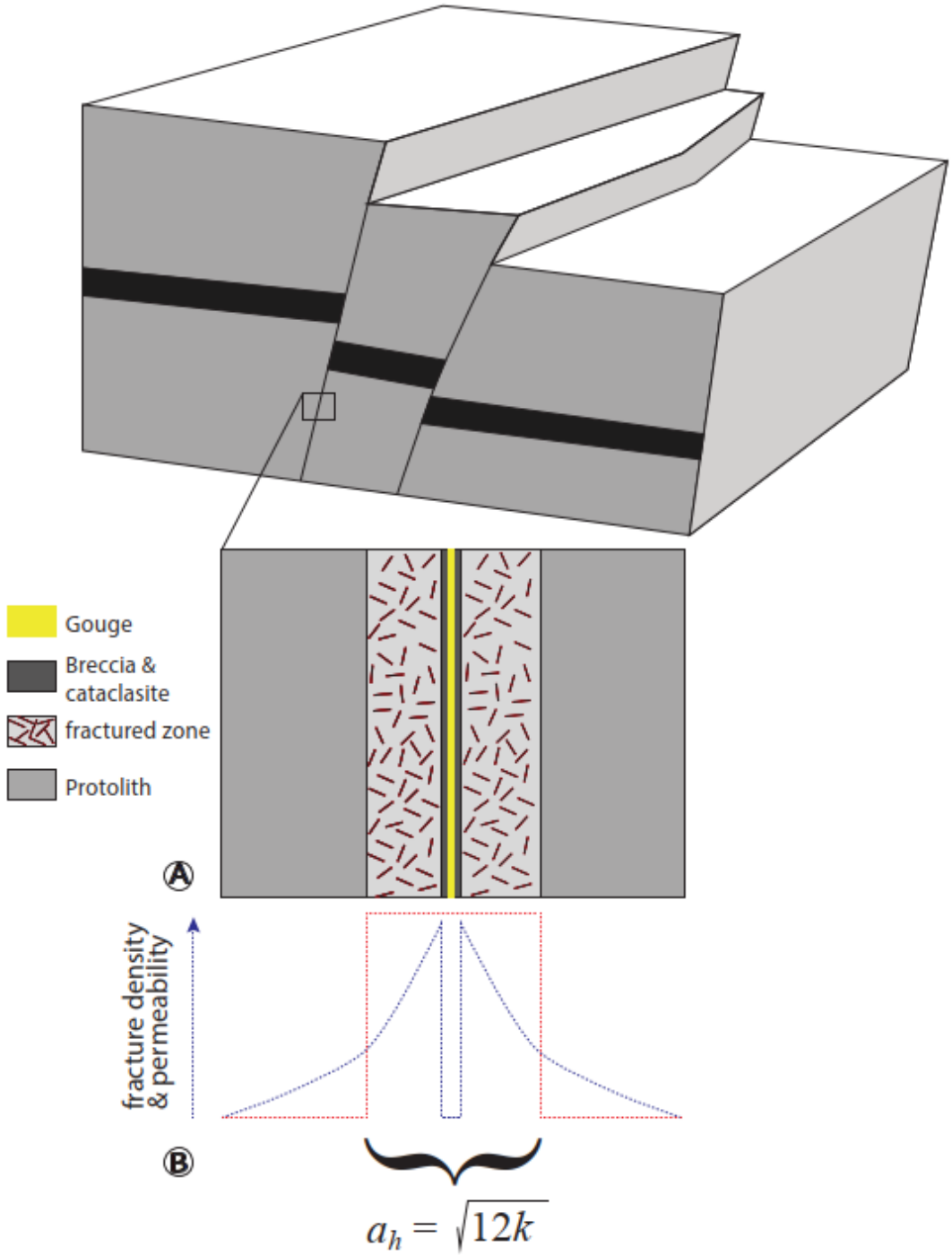


Fig. 3 A) Schematic diagram of fault zones and terminology; B) the permeability and fracture density of different fault zones (blue broken line), which is simplified by a homogeneous permeability value (red broken line).

Unlike the permeability of rock blocks, which is kept constant throughout the simulation, the fault permeabilities are related to their hydraulic aperture $a_h$ (Eq. 7) which can vary depending on their deformation. In 3DEC, three values define the effective hydraulic aperture of the faults: the maximum aperture ($a_{max}$) above which the hydraulic aperture is no longer related to the opening

(large deformation), the residual aperture ($a_{res}$) below which an increase in effective normal stress does not affect the permeability (closed state), and the initial aperture ($a_0$) is considered at the initial stage of the simulation. In addition, because the majority of faults associated with uranium deposits in the Athabasca Basin are nearly vertical (≈ 80˚; Eldursi et al., 2021a), and for simplification purposes the faults are vertical in all our models.

### 3.4 Dataset

All the mechanical and physical properties (e.g., density, porosity, and permeability) of basement and basin rock units are extracted from technical and internal reports provided by Orano Canada Inc. and the Geological Survey of Canada based on lab analysis of drill hole samples (e.g., Mwenifumbo et al. 2003; Harrison 2015). The fault mechanical properties (e.g., shear and normal stiffnesses, friction and dilation angles, cohesion, and tensile strength) are extracted from previous published works (e.g., Li et al., 2018; Eldursi et al., 2021a) that are approved by Orano Canada Inc.. Furthermore, the simplified orebodies' geometries and associated fracture networks are extracted from published works and internal technical reports that are approved by Orano Canada Inc. and the Geological Survey of Canada (e.g., Guffey et al. 2019; Benedicto 2018; IAEA 2018; Eldursi et al. 2021a).

## 4. Numerical results

The first two stages (mechanical on // fluid off, and mechanical off // fluid on) are only parts of the model preconditioning phase and used to reach the mechanical and hydraulic equilibriums (to assure a clean virgin state). Thus, all the following results are obtained during the third "last" stage of the numerical procedure (coupled stage "mechanical on // fluid on") where the fluid is injected from one side of the hydraulic fault (Fig. 2A).

In the model with 90˚ of intersection angle, only normal displacement (dilation) is observed along the hydraulic fault (Fig. 4A). The results are related to the applied boundary conditions, where the applied stresses $\sigma_h$ ($\sigma_x$) and $\sigma_H$ ($\sigma_y$) are parallel to x-, and y-axes, respectively (Fig. 2A). In the other models, decreasing the intersection angle (< 90˚) induces shear displacements along the natural fault (Fig. 4B).

Figures 5, 6, and 7 summarize the numerical results obtained for the normal and reverse faulting regimes. The results of the strike-slip regime are similar to those obtained under the reverse regime due to the high value of HDS (36, and 31 MPa respectively), therefore, they are not shown. In all models, three distinct behaviors are observed: the fluid either crosses the natural fault and continues along the hydraulic fault, diverts toward the natural fault, or stops at the intersection point. The latter behavior is only observed either when the pressure of injected fluid is less than 90% of the normal stress applied to the hydraulic fault ($\sigma_h$ ($\sigma_x$)) or when the basin permeability is higher than the initial fault permeability (initial aperture $a_0$). In this case, the injected fluid switches direction at the intersection zone from horizontal flow along the hydraulic fault to vertical flow toward the basin (Fig. 8).

In the normal faulting regime (Fig. 5), the fluid propagates along the hydraulic faults for models with intersection angles equal to 90˚, 70˚, 50˚, and 30˚. This is well demonstrated by the increase

of fault permeability (hydraulic aperture) up to the maximum assigned value (0.001 m), the tensile failure, and the establishment of a linear pressure gradient along the hydraulic fault.

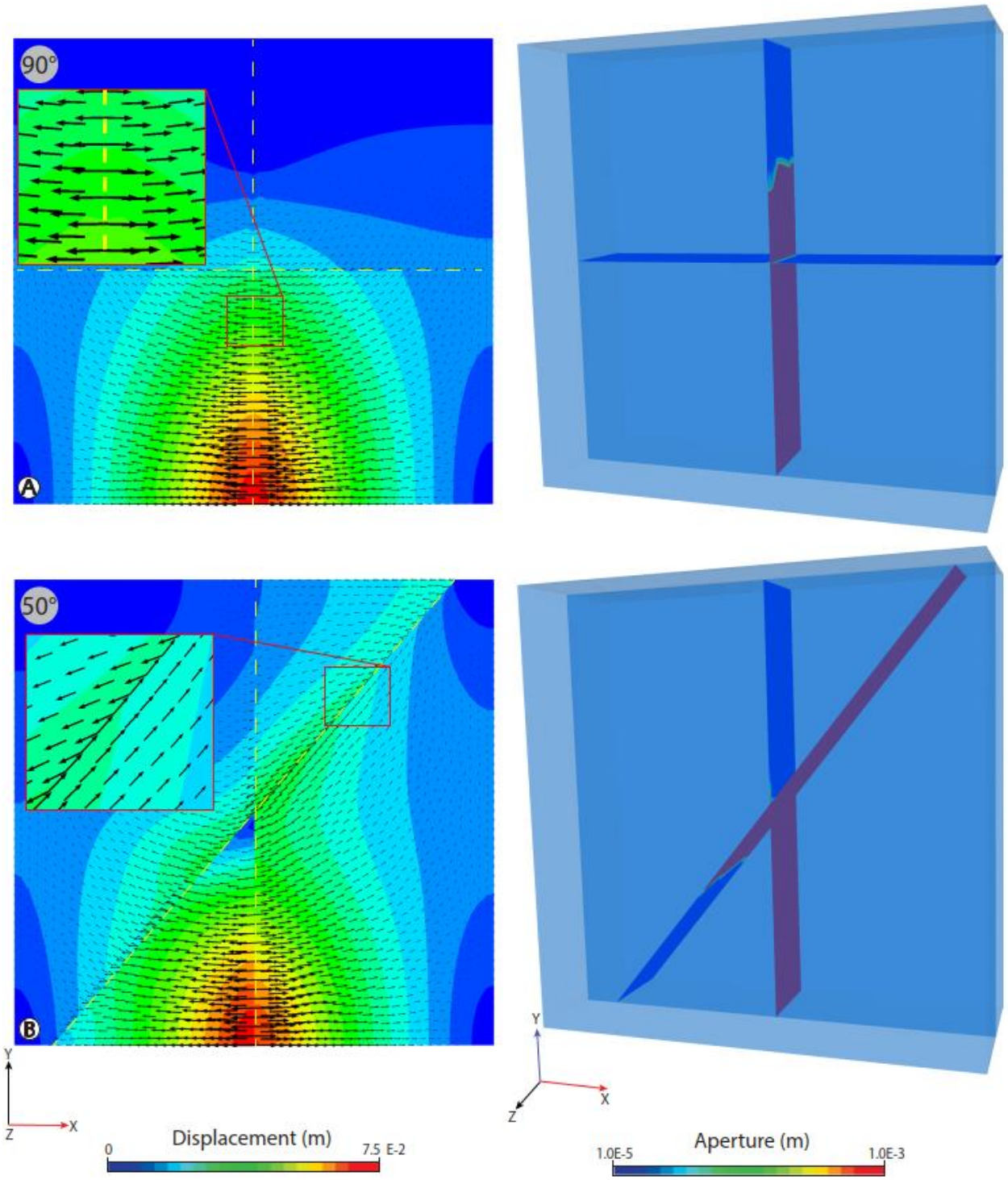


Fig. 4 Block displacement along the two faults due to the change in the intersection angle between the two faults A) at 90°, and B) 50° under reverse faulting regime.

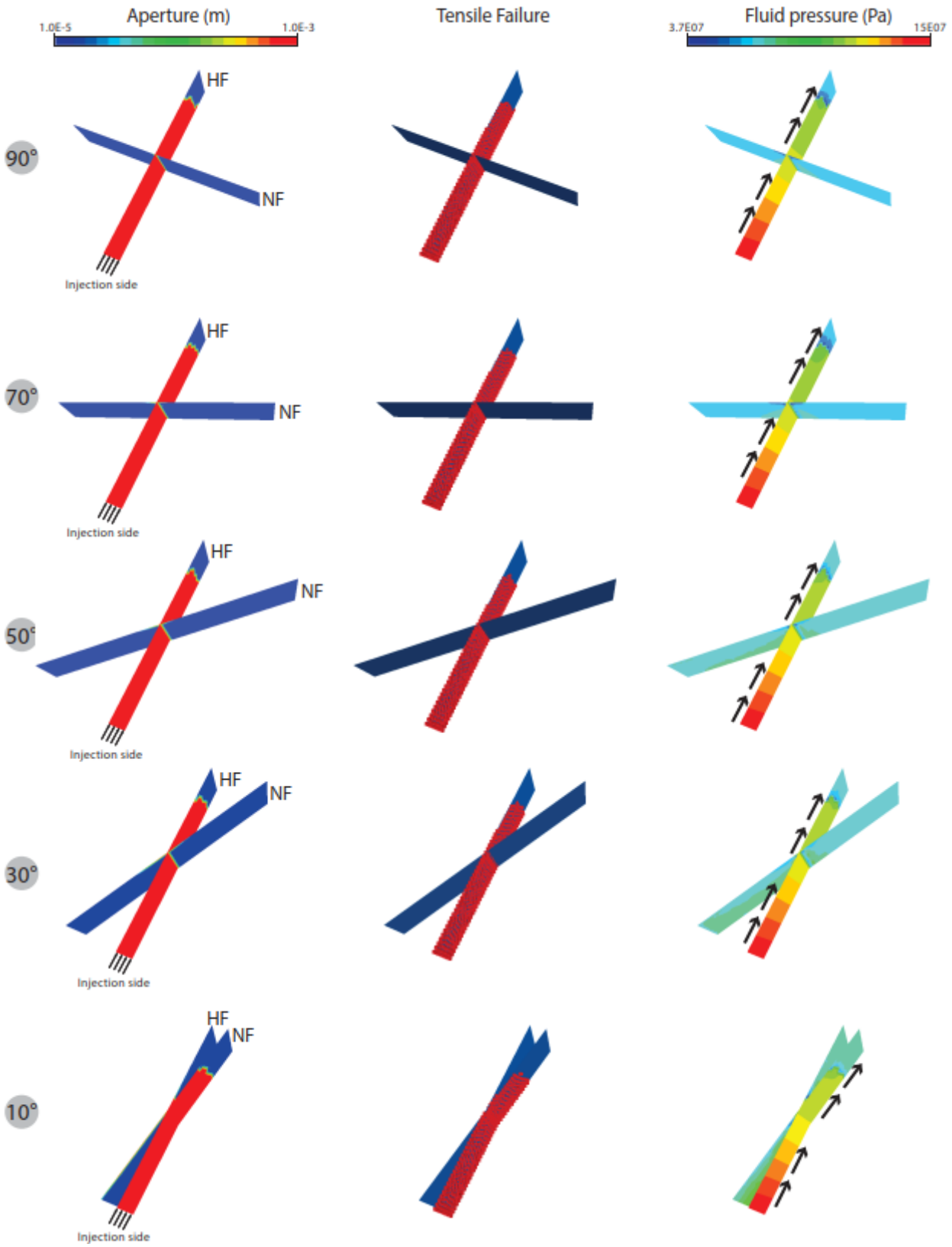


Fig. 5 Hydraulic aperture, tensile failure, and fluid pressure along the two faults of the primary models under normal faulting regime. (HF) hydraulic fault, (NF) natural fault.

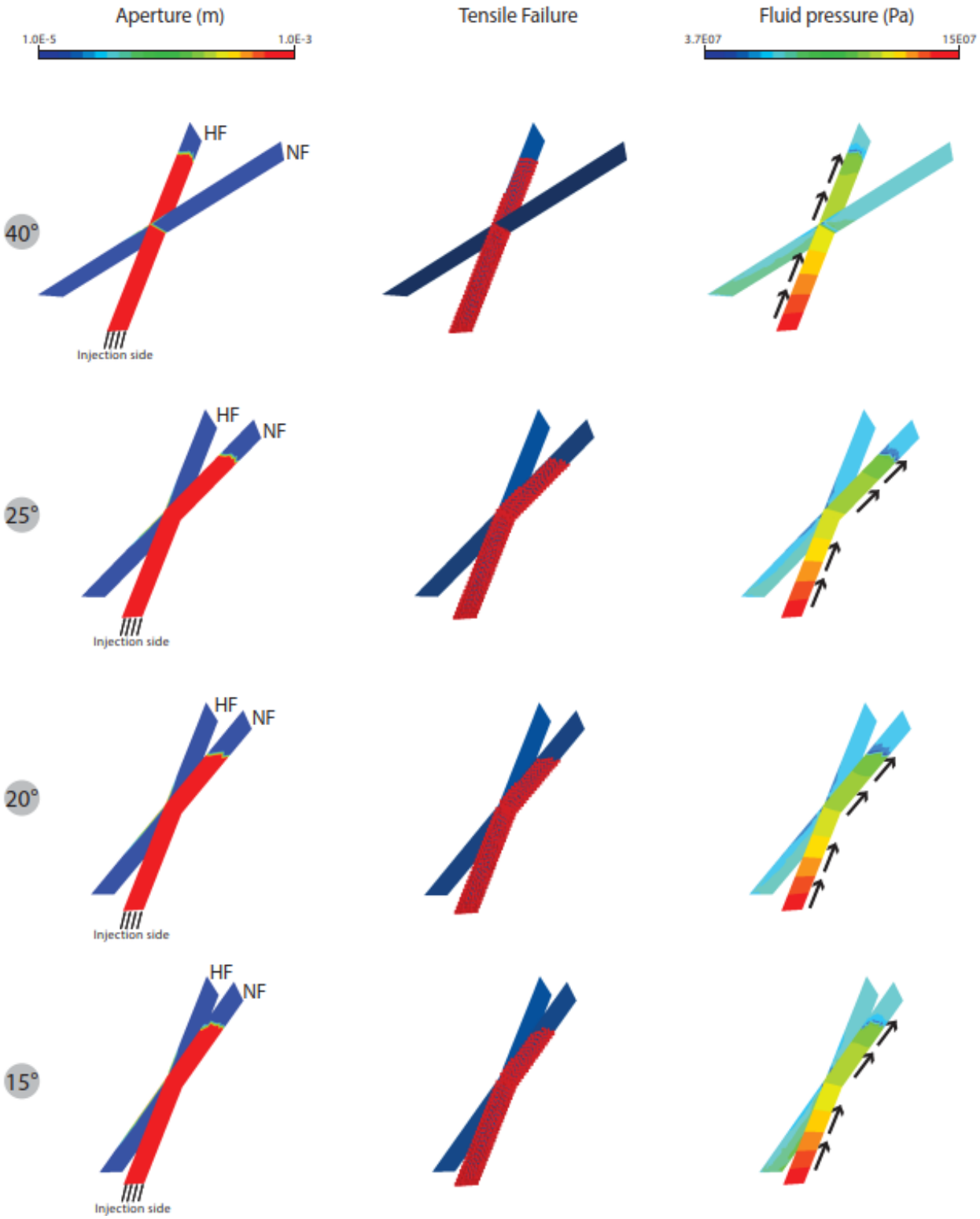


Fig. 6 Hydraulic aperture, tensile failure, and fluid pressure along the two faults of the supplementary models under normal faulting regime. (HF) hydraulic fault, (NF) natural fault.

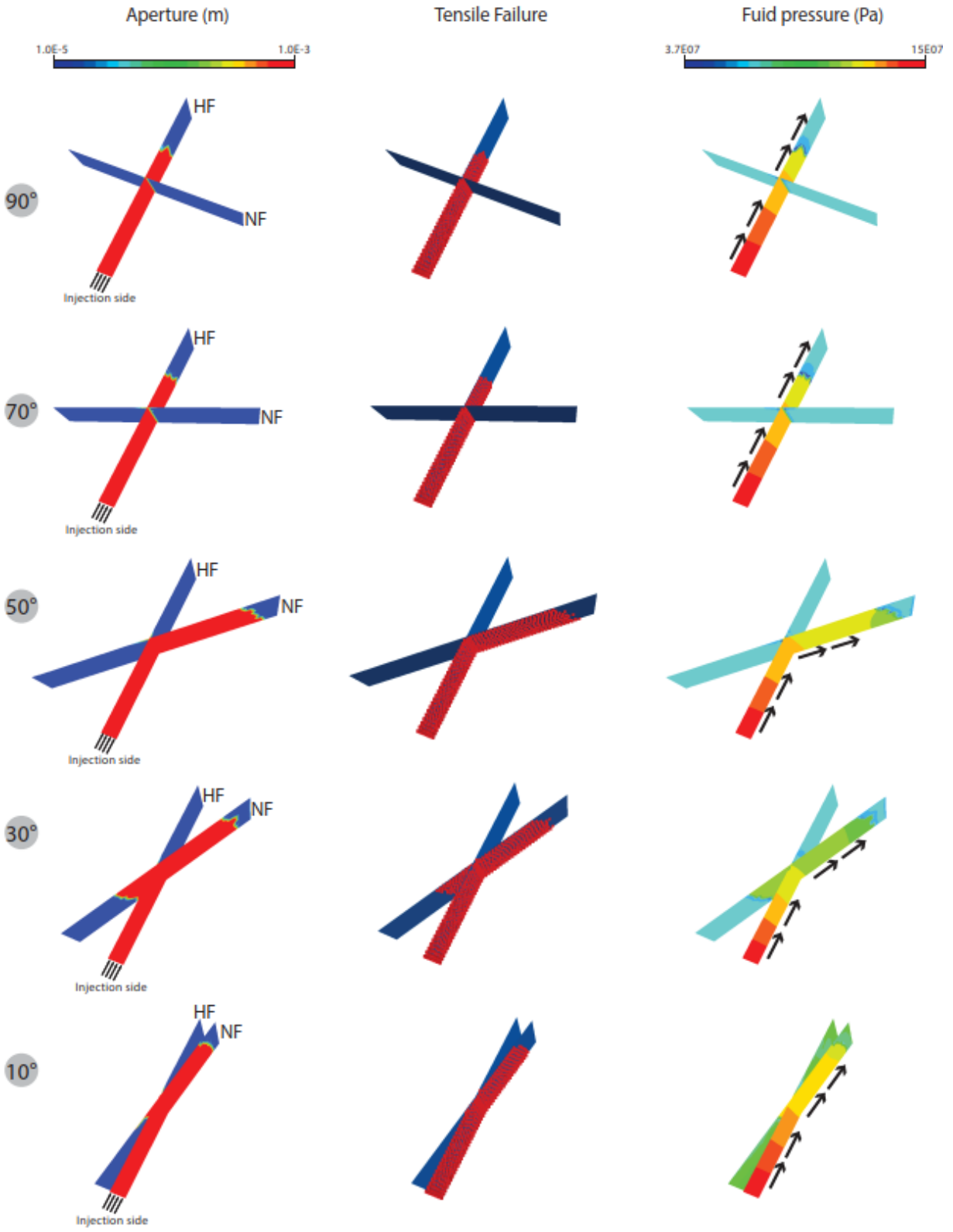


Fig. 7 Hydraulic aperture, tensile failure, and fluid pressure along the two faults of the primary models under reverse faulting regime. The results are consistent with those observed under strike-slip faulting regime. (HF) hydraulic fault, (NF) natural fault.

On the other hand, the fluid diverts toward the natural faults for an intersection angle equal to 10˚. To ensure that the results are not due to numerical errors, and to define accurately the critical intersection angle for the normal regime, supplementary models were run (40˚, 25˚, 20˚, and 15˚; Fig. 6). The results are consistent with those obtained with the primary models, confirming that the fluid diverts toward the natural fault for an intersection angle under circa 25˚ under a normal faulting regime. However, under strike-slip and reverse faulting regimes the critical intersection angle at which the fluid diverts toward the natural fault is around 50˚ (Fig. 7). Models of different burial depths do not have a significant effect on fluid flow patterns; therefore, the results are not shown.

## 5. Discussion

The effects of burial depth, basin permeability, and the injected fluid pressure on flow diversion at the intersection zone are evaluated. The pressure of injected fluid was restricted to $110\% \geq P_f > 90\%$ of $\sigma_h$ ($\sigma_x$), since values of fluid pressure less than 90% of $\sigma_h$ ($\sigma_x$) can not overcome the normal stress ($\sigma_h$ ($\sigma_x$)) applied to the hydraulic fault, and therefore can not open the hydraulic fault. A basin permeability higher than the initial fault permeability ($a_0$) leads the injected fluid to flow upward toward the basin as an easiest flow path rather than overcome the applied normal stress around the intersection zone (Fig. 8). As the applied stresses in all faulting regimes are calculated based on the estimated vertical "overburden" load ($\sigma_v$ ($\sigma_z$)), the changes in burial depth from 6000 m to 3000 m (Table 2) does not show surprising results.

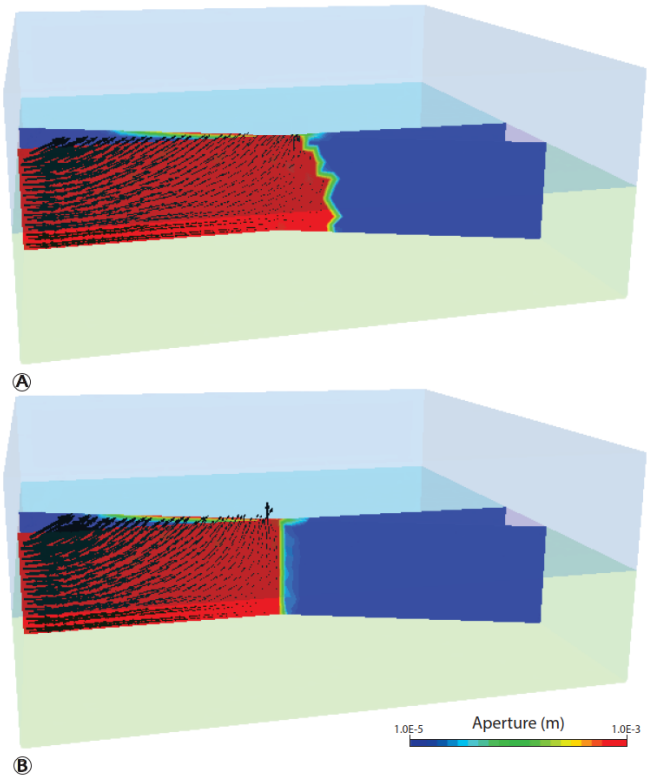


Fig. 8 The model 20˚ of approaching angle under normal faulting regime. A) with basin permeability equal to the initial fault aperture (2E-10 $m^2$); B) basin permeability is higher than the initial fault aperture (4E-10 $m^2$).

Fault failure modes can range between tensile, hybrid, and shear based on stress conditions and rock properties (Ferrill et al., 2019, 2020). Tensile failure is characterized by normal displacement perpendicular to the fault walls (dilation) without significant displacements parallel to the fault plane (shear displacement). This type of dilation is well observed along the hydraulic fault where the fluid is injected (Fig. 4A). Shear (or slip) failure is associated to a displacement parallel to the fault plane (Fig. 4B), accompanied with dilation. Shear failure occurs along the natural fault when the intersection angle is < 90˚. A hybrid failure mode corresponds to a transitional mode between the two aforementioned modes (Fig. 4B; Ferrill et al., 2019).

In the 'slip/dilation tendencies analysis' (Ferrill et al., 2019), the tensile mode is well demonstrated along the hydraulic fault in the case of 90˚ of intersection angle as $\sigma_h$ and $\sigma_H$ are parallel to the x-, and y-axes respectively. In this case, only normal stresses develop along both faults while shear stress being negligible, leading the hydraulic fault to open with non-slip tendency. As the magnitude and directions of principal stresses change along the natural fault (intersection angles < 90˚), the natural fault tends to activate in hybrid to shear modes, as the slip tendency gradually increases. However, dilation tendency remains present in the two modes (Rutqvist, 2015; Meixner et al., 2016; Schofield, 2016; Ferrill et al., 2020).

The stress conditions (magnitudes, and directions) hence control how fluid deviates from one fault to another. The contributions of normal and shear stresses to fault dilation, based on the obtained numerical results, are discussed below.

**5.1 Effects of normal stress and HDS**

In all the models, fluid propagation (during the fully-coupled stage) along the faults and through the intersection zone can be divided into three phases. Figure 9 details the three phases for the model '50˚ of intersection angle' under the normal faulting regime. The resulting curves include fluid pressure at the intersection point and effective normal stress at recording points 4 and 7 (first, and third contact; Fig. 2B) that are located just after the intersection point in the hydraulic and natural faults, respectively (Fig. 9A). Figure 9B shows the normal displacements at the same points. The first phase is characterized by a hydrostatic fluid pressure along the hydraulic fault up to the intersection point. This stage ends with an obvious drop in fluid pressure at the intersection point resulting from the opening of the first part of the hydraulic fault (Fig. 9). In the second phase, the fluid accumulates at the intersection point. The fluid pressure rises and normal displacement increases synchronously, indicating that the fluid pressure had overcome the effective normal stress at the intersection point (Fig. 9A and B). However, it is also observed that the increase of fluid pressure is associated with an explicit change in effective normal stress at points 4 and 7 (Fig. 9A). The end of the second phase is distinguished by a second drop in fluid pressure as the fluid pressure reaches a critical value at which the fluid pressure is sufficiently high to open the fault at the intersection point. During the third phase, the fluid crosses the intersection point and continues to propagate along the hydraulic fault as indicated by an increase in the normal displacement simultaneously with a decrease of the effective normal stress at point 4. Synchronously, the normal displacement at point 7 decreases as the effective normal stress increases at point 7.

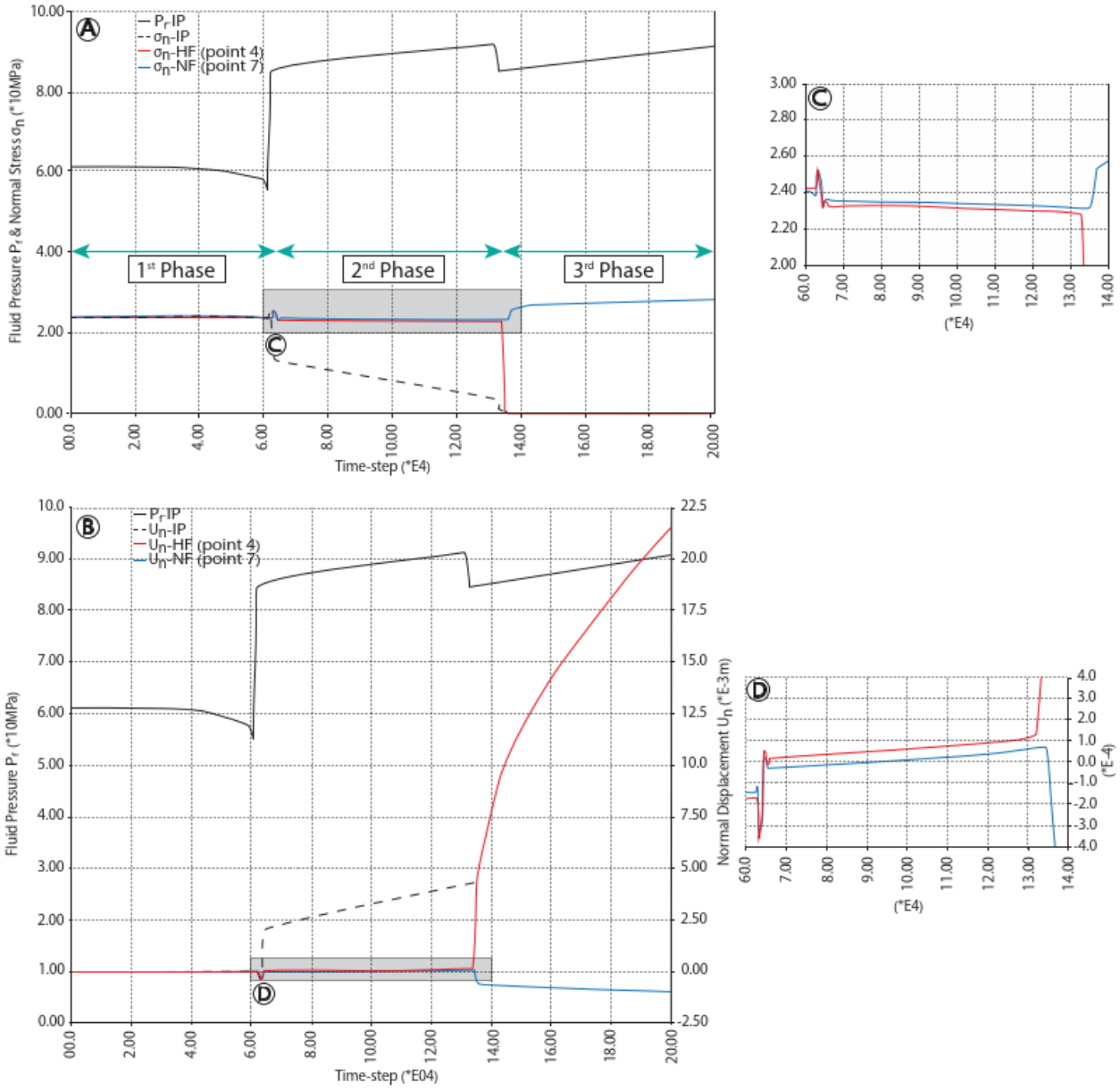


Fig. 9 A) Change in fluid pressure ($P_f$) at the intersection point (IP), and corresponding change in normal stress ($\sigma_n$) at the intersection point (IP), and observation points (4 and 7). B) Change in fluid pressure ($P_f$) at the intersection point, and corresponding changes in normal displacement at the intersection point, and observation points (4 and 7). The data are extracted from model 50° of intersection angle under normal faulting regime; (HF) hydraulic fault, (NF) natural fault. Note that the right vertical axis is reserved for normal displacement values (m), while the left vertical axis is dedicated for fluid pressure values (*10 MPa).

To better understand the results, the effective normal stress and normal displacement at points 4 and 7 have been measured at the end of phase two, when the fluid reaches the intersection point, and just before the fluid propagates toward either the second part of the hydraulic fault or diverts toward the natural fault (Fig. 10). Under a normal faulting regime, in the model with the

intersection angle equal to 90˚, the fluid propagates along the hydraulic fault, while the natural fault remains closed as it is subjected to higher normal stress ($\sigma_H = \sigma_y$). As the intersection angle decreases, the effective normal stress along the natural fault decreases gradually, leading to an increase in the normal displacement (Figs. 10A and B). Based on the plotted data (effective normal stress and normal displacement versus intersection angle), the curves for normal stress and displacement at both points cross each other at an angle of circa 27˚, which is considered to be a critical angle at which the fluid diverts toward the natural fault.

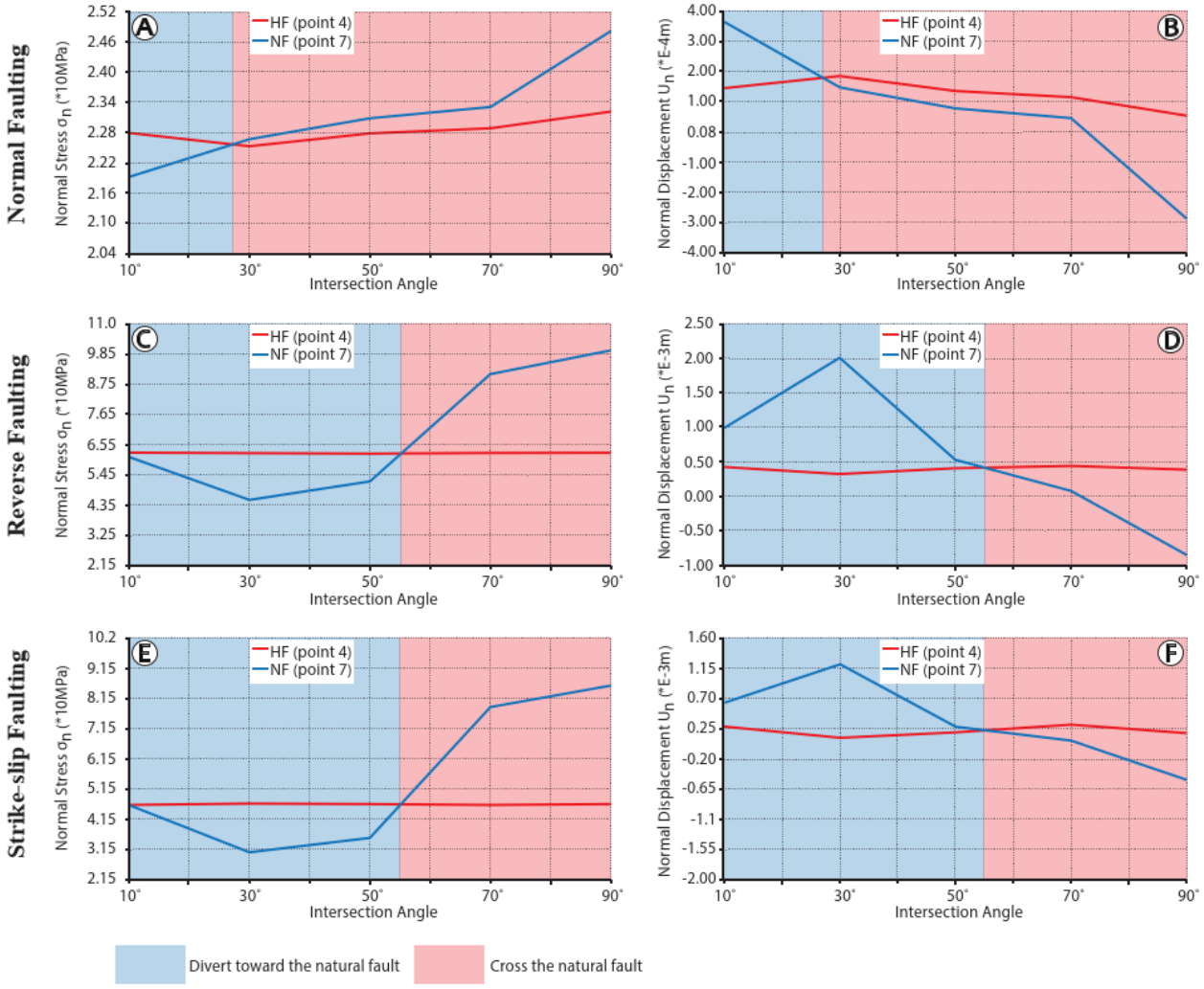


Fig. 10 Variations of normal stress and displacement at points 4 and 7 for different intersection angles at a given time (end of 2nd phase) for each faulting regime; (HF) hydraulic fault, (NF) natural fault.

Under reverse and strike-slip faulting regimes, the HDS is equal to 31MPa and 36MPa respectively, instead of the 5MPa used for the normal faulting regime. As the intersection angle decreases, $\sigma_H$ is no longer perpendicular to the natural fault, facilitating the dilation and activation of the natural fault at a higher intersection angle (around 50˚) due to the increase in shear stress. The critical intersection angle at which the fluid diverts toward the natural fracture is determined

to be 55˚ according to Figure 10C−F. Overall, as the intersection angle declines, the effective normal stress along the natural fault gradually decreases. Once the critical intersection angle is reached, the effective normal stress along the natural fault becomes smaller than that along the hydraulic fault, enabling the fluid to divert toward the natural fault.

Figure 11 shows the changes over time of both the effective normal and shear stresses induced by fluid propagation in the Mohr plane for the model '50˚ of intersection angle' under the three faulting regimes. This model was chosen as the fluid behaves differently under different faulting regimes. While the fluid continues to propagate along the hydraulic fault under a normal faulting regime, it deviates toward the natural fault under reverse and strike-slip faulting regimes. However, a similar stress-path is observed for activated faults (the hydraulic fault under normal regime (Fig. 11A) or the natural fault under reverse or strike-slip regimes (Fig. 11B, and C)). The stress-path can be divided into three parts: 1) the effective normal stress decreases slightly in conjunction with the shear stress due to fluid propagation until the fluid pressure front reaches the observation point (denoted by a black square in Fig. 11); 2) rupture occurs, leading to a significant decrease of the effective normal stress due to the increase of the fluid pressure while the shear stress remains nearly constant; and 3) the shear stress decreases in conjunction with the effective normal stress as the fault dilates and slips, leading its aperture to significantly increase.

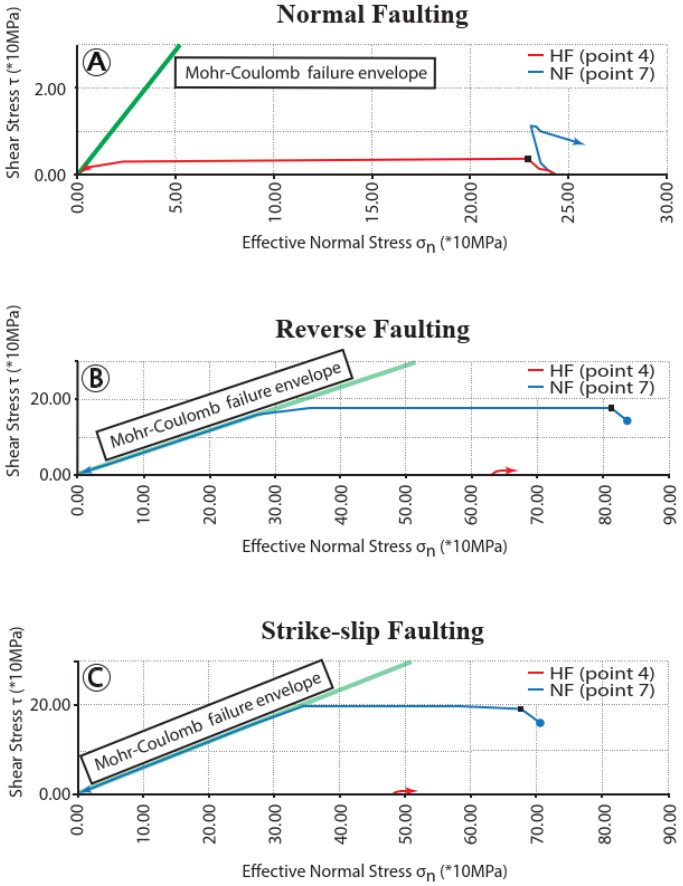


Fig. 11 Mohr-Coulomb failure envelope, and stress paths followed during the injection; the data are extracted from model 50˚ of intersection angle under each faulting regime at the observation points (4, and 7). The black square indicates the arrival of injected fluid at the observation point; (HF) hydraulic fault, (NF) natural fault.

Conversely to the normal faulting regime, the maximum stress ($\sigma_1$) is horizontal ($\sigma_H = \sigma_y$) under reverse and strike-slip faulting regimes. Under these regimes, and once the intersection angle is lower than 90˚, $\sigma_1$ ($\sigma_H = \sigma_y$) is inclined to the natural fault. This position significantly increases the shear stress along the natural fault which, in turn, facilitates the activation of the fault in shear mode (fault slip mode) due to lateral movement parallel to the fault wall. Figure 12 displays the variation in shear stress along the natural and hydraulic faults for the three regimes at the two observation points (4 and 7; Fig. 2B). Although the applied horizontal stresses and the injection pressure vary between the three cases, the ratio between the fluid pressure peak and the maximum shear stress at the end of the second phase is higher in the reverse and strike-slip regimes compared to those observed in the normal faulting regime: the natural fault dilates more easily when the HDS is high. Thus, the HDS is apparently another physical clue that controls the fluid deviation from the hydraulic fault toward the natural fault at the intersection zone.

Several experimental and numerical studies have been performed to assess hydraulically-induced fracturing in oil and gas reservoirs (e.g., Blanton, 1982; Gu et al., 2012; Chuprakov et al., 2014; Guo et al., 2015; Dehghan et al., 2016; Zou et al., 2016; Ma et al., 2017; Duo et al., 2019; Hu et al., 2020; Zhang et al., 2020; Li et al., 2021). For instance, Blanton (1982) and Gu et al. (2012) suggested an HDS-intersection angle criterion based on lab experiments on shale and hydrostone-plaster block samples. The criterion describes the fluid propagation model based on the relation between HDS and the intersection angle. The experiments were carried out under mechanical conditions similar to the normal faulting regime ($\sigma_1$ vertical to the block sample ($\sigma_z$)) and the intersection angle was varied between 30˚, 45˚, 60˚, and 90˚. However, as the fluid properties (e.g., fluid viscosity) were unclear, Chuprakov et al. (2014) evaluated different values of fluid viscosity (0.001, 0.1, and 1 Pa s) and demonstrated that the criteria proposed by Blanton can be significantly affected. Other studies were performed, mainly using numerical modeling techniques (e.g., Guo et al., 2015; Dehghan et al., 2016; Zou et al., 2016; Ma et al., 2017; Dou et al., 2019; Hu et al., 2020; Zhang et al., 2020; Li et al., 2021). Although the findings and criteria vary from one study to another due to variations in conditions used (e.g., high fluid viscosity, injection rate), the results, in general, emphasize that the diversion of fluid toward the natural fracture decreases with an increase in the HDS. This conclusion is in discrepancy with the findings of the present study (direct proportion between HDS and intersection angle). However, it is delicate to compare their findings with the present results for the following three reasons: 1) the experimental studies (e.g., Blaton, 1982, and Gu et al., 2014) evaluated the effect of HDS variations on the critical intersection angle only in a context similar to a normal faulting regime ($\sigma_1$ is the vertical applied stress ($\sigma_v$)) and the minimum evaluated intersection angle was 30˚, while according to our results, the critical intersection angle at which the fluid diverts toward the natural fault is lower than that, circa 27˚ at HDS equal to 5MPa; 2) in the previous numerical modeling studies, the three stress components were not considered either due to the use of 2-D models (e.g., Guo et al., 2015; Duo et al., 2019), or of plane strain conditions (Hu et al., 2020); and 3) because their focuses were on productivity enhancement of oil and gas reservoirs, hence artificial conditions were applied to

observe their influences on fracture propagation (e.g., Zou et al., 2016; Ma et al., 2017; Zhang et al., 2020; Li et al., 2021).

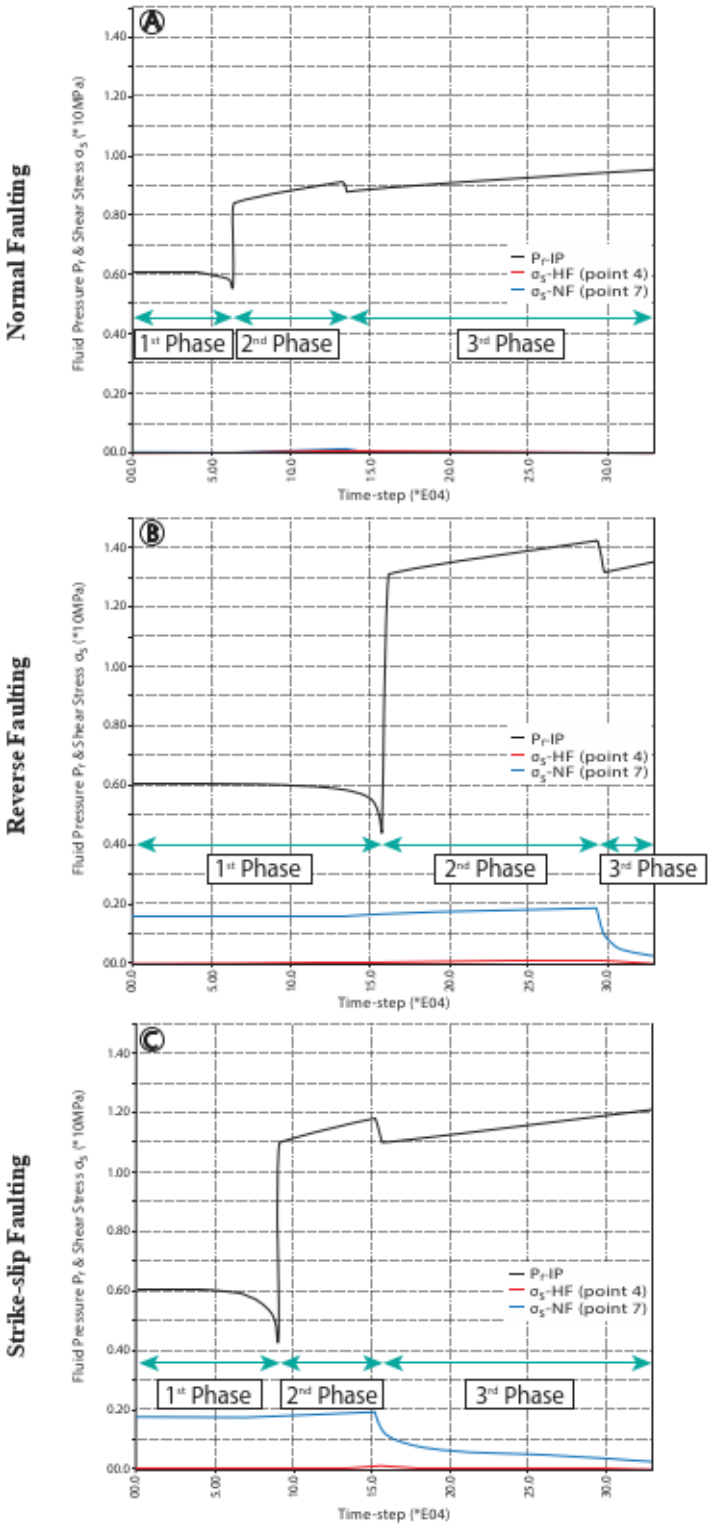


Fig. 12 Change of fluid pressure ($P_f$) at the intersection point (IP), and corresponding changes in shear stress ($\sigma_S$) at the two observation points under different faulting regimes; (HF) hydraulic fault, (NF) natural fault.

### 5.2 Implications for the formation of structurally-controlled mineral deposits

As noted above, the structurally-controlled URU deposits in the Athabasca Basin comprise monometallic breccia- and/or vein-associated basement-hosted to polymetallic basin-hosted deposits, both associated with cataclastic breccia and fracture zones. They are found at the intersection zone of two or more fault arrays and are associated with reverse and strike-slip faults that have been reactivated episodically under a compressional regime (e.g., Annesley et al., 2005; Jefferson et al., 2007; Martz et al., 2017, 2019 among others). Therefore, the field observations can be compared to the numerical results that were obtained under reverse and strike-slip faulting regimes (Fig, 7). Although the geometries of different mineral deposits in the eastern part of the basin are provided (Fig. 1A), information on the associated fault networks is scarce.

Figure (13) shows four mineral deposits and associated fracture networks at the deposit scale in the eastern part of the Athabasca Basin. As described by Guffey et al. (2019), three pre-existing fault sets are associated with the McArthur River U deposit (Fig. 13A), including a graphite-bearing reverse fault P2, striking 45˚, and dipping 40˚–60˚ SE along which the uranium has precipitated. The fault system also includes two other nearly vertical fault sets striking NNW and NW, respectively. From the results of the present study, the critical intersection angle at which the fluid diverts from the hydraulic fault toward the intersecting fault is 55˚ for both reverse and strike-slip faulting regimes. In the McArthur River area, as the intersection angle is higher than 50˚, the U-bearing fluid probably circulated along P2, and crossed the two secondary faults (NNW and NW faults, Fig. 13A), leading to precipitation of uranium along the P2 fault.

Based on a detailed study by Benedicto (2018), the Midwest U deposit area hosts four fault sets: two major fault sets (NE-SW graphitic mineralized shear zones and N-S trending faults) and two subsidiary faults (oriented E-W, and NW-SE; Fig. 13B). However, the N-S and NW-SE fault sets are younger than the mineralization (Benedicto, 2018), so the mineralizing fluid is presumed to have accumulated along the NE-SW faults, resulting in the formation of the Midwest Main deposit. At the intersection zone, the mineralizing fluid was diverted toward the second NE-SW fault to form the NE deposit (Midwest A), as the angle between the two NE-SW fault sets is 32˚ (based on the provided map). In the Collins Bay area, the IAEA (2018) published a map that showed two sets of faults (NE and NW faults; Fig. 13C). There, the Collins Bay B-Zone U deposit is located along a NW relay between two strands of the NE structure. Fluid flow could have diverted at the intersection zones from the NE fault toward the NW fault and also from the NW fault toward the NE fault. The angles between the two are inferior to the critical angle of 55˚.

In the Cigar Lake area, Martz et al. (2017, 2019) and Eldursi et al. (2021a) used a 3-D detailed model (based on drillhole and field data) to illustrate four fault sets: E-W graphitic-bearing faults that are associated with the U deposit and subsidiary steeply-dipping to subvertical NE-SW, NW-SE, and N-S faults (Fig. 13C). Based on fluid inclusion planes (FIPs, Martz et al., 2017), only two fault sets were active during the formation of the U deposit (NE and E-W fault sets). So, in the Cigar Lake area, we presume that the NE fault was the hydraulic fault along which the basement fluid invaded the system at the local scale based on the following points:

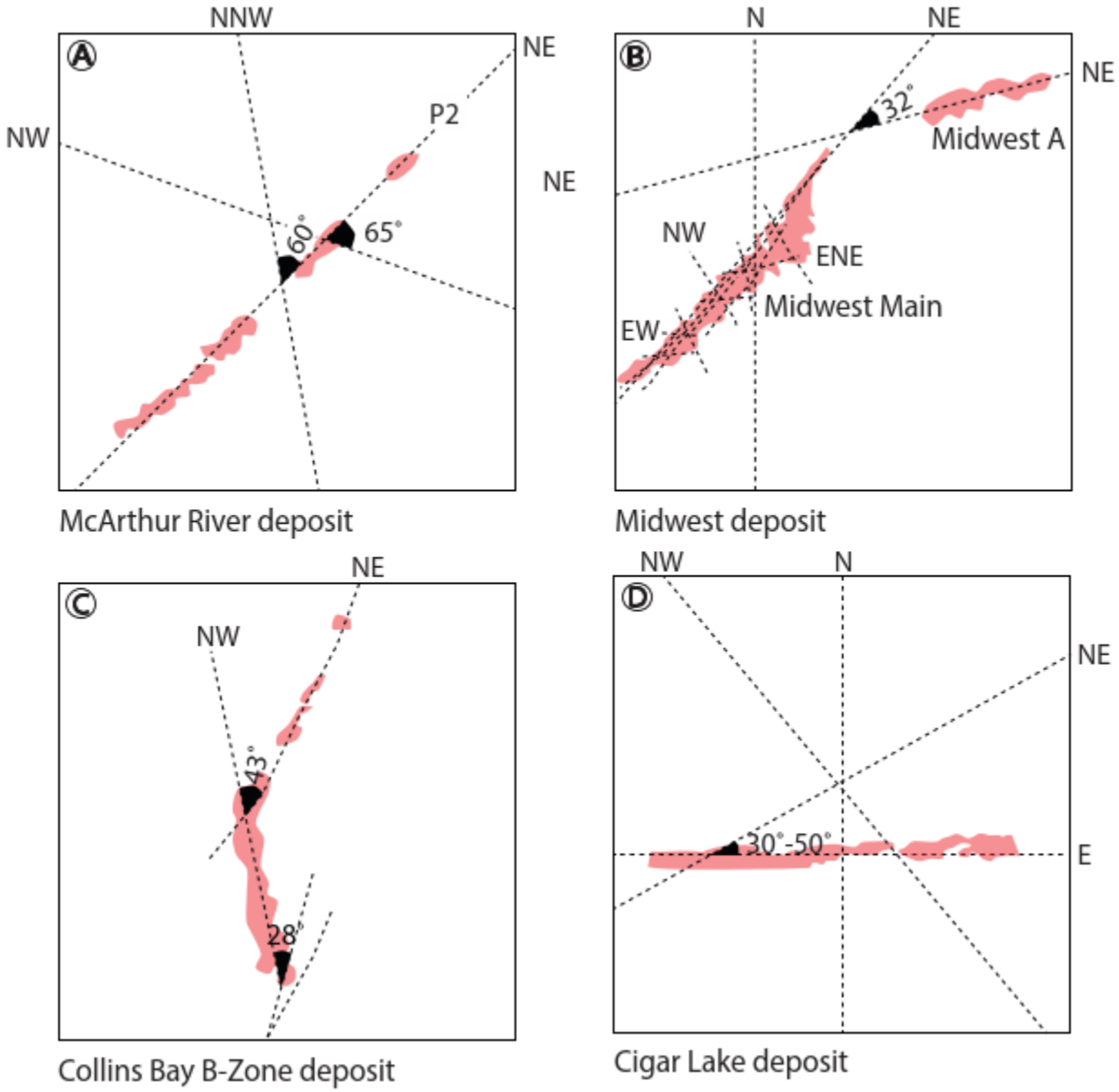


Fig. 13 The simplified fault network at the local scale for different uranium deposits in the Athabasca Basin (Guffey et al. 2017; Benedicto 2018; IAEA 2018; Eldursi et al. 2021); the angles indicate the intersection angles between faults. The deposits are not to scale.

a) More than 65% of the discovered uranium deposits are oriented NE (Thomas et al., 2016, Fig. 1A).
b) The regional fluid flow patterns are oriented NE (Fig. 1C; Earle and Sopuck, 1989).
c) The NE fault hosts U deposits near the Cigar Lake area (e.g., the P2 fault at McArthur River, and Christie Lake deposits; Fig. 1A #1 and #11).
d) And most importantly, Martz et al. (2017) demonstrated that the fluid inclusion planes (FIPs) located in the NE-SW fault are distinguished by trapped NaCl-rich fluid and traces of $CO_2$, $CH_4$ and $N_2$ that are characteristic of basement fluids.

Therefore, the U-bearing fluid diverted toward the E-W basement faults at the intersection zone, as the angle between the two-fault sets are less than the critical angle. This fluid then mixed with basinal fluid to form the deposits immediately above the unconformity surface during a long period of tectonic quiescence (Eldursi et al., 2021a).

Although, as seen above, the numerical results are consistent with field observations, the present study does not consider certain physical factors such as fault dip, variations in the rheology and mechanical properties due to heterogeneity of basement lithologies, and presence of a complex fracture network, which can potentially affect fault reactivation, and thus fluid propagation.

## 6. Conclusion

Although many numerical modeling studies have been performed to improve the understanding of the formation of unconformity-related basin-basement mineral deposits, the hydromechanical responses of faults at intersection zones and their potential roles in controlling fluid pathways and the formation of oriented mineral deposits have been barely discussed or demonstrated numerically. The present study uses hydromechanically-coupled numerical simulations to provide new and significant insights into the formation of oriented basin/basement interface metallic mineral deposits at intersection zones. The results are strongly coherent with field observations from URU deposits in the Athabasca Basin, and highlight the role of fault intersections on the formation of oriented mineral deposits, due to their structural control on the hydraulic flow system:

1. Fluid can: a) be stopped at the intersection zone between hydraulic and natural faults; b) cross the natural fault and continue along the hydraulic fault, or c) divert toward the natural fault at the intersection zone.
2. The variation of effective normal stress along faults is the main factor that affects the fluid deviation at the intersection zone.
3. Depending on the faulting regime, the critical intersection angle at which the fluid crosses or diverts toward the natural fault varies between circa 27˚ to circa 55˚ for normal and for reverse or strike-slip faulting regimes respectively.
4. The variation of the critical intersection angle in different faulting regimes relies mainly on the Horizontal Differential Stress (HDS). The critical angle increases as the HDS increases.
5. With the conditions applied in the simulations, the fluid stops at the intersection zone either because the fluid pressure is less than 90% of the normal stress applied to the hydraulic fault, or because the basin permeability is higher than the initial fault permeability.
6. Burial depth and fluid pressure (at geological and natural conditions) do not significantly affect fluid propagation and diversion.

**Acknowledgment**:

This work is a part of the THM (Thermal-Hydraulic-Mechanical) Project in the GeoRessources department of the University of Lorraine (France). The project is supported financially and technically by Orano. A part of this work has been also supported by the French National Research Agency through the national program “Investissements d’avenir” with the reference ANR-10-

LABX-21-01/ LABEX RESSOURCES21. The authors thank David Quirt, formerly with Orano Canada, for his editing, constructive remarks, and advice to improve the manuscript.

**References:**

Anderson, E.M., 1951. The dynamics of faulting, 2nd ed. Olivier & Boyd, Edinburgh Geological Society. https://doi.org/10.1144/transed.8.3.387

Annesley, I.R., Madore, C., Portella, P., 2005. Geology and thermotectonic evolution of the western margin of the Trans-Hudson Orogen: evidence from the eastern sub-Athabasca basement, Saskatchewan. Canadian Journal of Earth Sciences. 42, 573–597. https://doi.org/10.1139/e05-034

Alexandre, P., Kyser, K., Jiricka, D., 2009. Critical Geochemical and Mineralogical Factors for the Formation of Unconformity-Related Uranium Deposits: Comparison between Barren and Mineralized Systems in the Athabasca Basin, Canada. Economic Geology. 104, 413–435. https://doi.org/10.2113/gsecongeo.104.3.413

Aquilina, L., Boulvais, P., Mossmann, J., 2011. Fluid migration at the basement/sediment interface along the margin of the Southeast basin (France): implications for Pb–Zn ore formation. Mineralium Deposita. 46, 959–979. https://doi.org/10.1007/s00126-011-0360-9

Benedicto, A., 2018. Report Mission July 2018 Midwest (Main) project, internal report 2018-10-R04 18 Orano p.

Benedicto, A., Abdelrazek, M., Ledru, P., MacKay, C., Kinar, D., 2021. Structural Controls of Uranium Mineralization in the Basement of the Athabasca Basin, Saskatchewan, Canada: Geofluids v. 2021, Article ID 3853468, p. 30. https://doi.org/10.1155/2021/3853468

Berg, S.S., Skar T., 2005. Controls on damage zone asymmetry of a normal fault zone: outcrop analyses of a segment of the Moab fault, SE Utah. Journal of Structural Geology. 27, 1803–1822. https://doi:10.1016/j.jsg.2005.04.012

Biot, M.A., 1956. General Solutions of the Equations of Elasticity and Consolidation for a Porous Material. The Journal of Applied Mechanics. 23(1), 91–96. https://doi.org/10.1115/1.4011213

Blanton, T.L., 1982. An experimental study of interaction between hydraulically induced and pre-existing fractures. In: Paper Presented at the SPE Unconventional Gas Recovery Symposium, Pittsburgh, Pennsylvania, 16–18 May. Paper Number: SPE-10847-MS. https://doi.org/10.2118/10847-MS

Boulanger, R.A., 2012. Geological, petrographic and geochemical characterization of the Roughrider West Zone unconformity-type uranium deposit, Athabasca Basin: Saskatchewan, Canada, M.Sc. Thesis, The University of Regina, 292 p. http://hdl.handle.net/10294/3618

Budhu, M., 2010. Soil mechanics and foundations: 3rd ed., John Wiley & Sons, USA, 780 p.

Caine, J. S., Evans, J. P., Forster, C. B., 1996. Fault zone architecture and permeability structure. Geology. 24(11), 1025–1028. https://doi.org/10.1130/0091-7613(1996)024<1025:FZAAPS>2.3.CO;2

Cappa, F., Guglielmi, Y., Nussbaum, C., Birkholzer, J. 2018. On the relationship between fault permeability increases, induced stress perturbation, and the growth of aseismic slip during fluid injection. Geophysical Research Letters. 45, 11,012–11,020. https://doi.org/10.1029/2018GL080233

Card, C.D., Campbell, J.E., Slimmon, W.L., 2003. Basement lithologic framework and structural features of the western Athabasca Basin; in Summary of Investigations 2003, Volume 2, Saskatchewan Geological Survey, Sask. Industry Resources, Misc. Rep. 2003-4.2, CD-ROM, Paper D-3, 17 p.

Card, C.D., Pană, D., Stern, R.A., Rayner, N., 2007. New insights into the geological history of the basement rocks to the southwestern Athabasca Basin, Saskatchewan and Alberta, in Jefferson, C.W. and Delaney, G., eds., EXTECH IV: Geology and Uranium EXploration TECHnology of the Proterozoic Athabasca Basin, Saskatchewan and Alberta: Bulletin 588: Geological Survey of Canada (also Special Publication 18: Saskatchewan Geological Society, Special Publication 4: Geological Association of Canada, Mineral Deposits Division), 119–134.

Card, C.D, Rayner, N., Pearson, G., Luo, Y., Creaser, R., 2018. Geochronological results from the southern Athabasca Basin region, Saskatchewan; in Summary of investigations 2018, Volume 2, Saskatchewan Geological Survey, Saskatchewan Ministry of Energy and Resources, Miscellaneous Report 2018–4.2, Paper A-4, 15 p.

Cheng, W., Jin, Y., Chen, M., XU, T., Zhang Y., Diao, C., 2014. A criterion for identifying hydraulic fractures crossing natural fractures in 3D space. Petroleum Exploration and Development. 41(3), 371–376. https://doi.org/10.1016/S1876-3804(14)60042-2

Chen, Z., 2012. Finite element modelling of viscosity-dominated hydraulic fractures: Journal of Petroleum Science and Engineering, v. 88–89, p. 136–144. https://doi.org/10.1016/j.petrol.2011.12.021

Chi, G., Li, Z., Chu, H., Bethune, K.M., Quirt, D., Ledru, P., Normand, C., Card, C., Bosman, S., Davis, W.J., Potter, E.G., 2018. A shallow-burial mineralization model for the unconformity-related uranium deposits in the Athabasca basin. Economic Geology. 113, 1209–1217. https://doi.org/10.5382/econgeo.2018.4588

Childs, C., Manzocchi, T., Walsh, J.J., Bonson, C.G., Nicol A., Schöpfer, M.P.J., 2009. A geometric model of fault zone and fault rock thickness variations. Journal of Structural Geology. 31. 117–127. https://doi:10.1016/j.jsg.2008.08.009

Chuprakov, D., Melchaeva, O., Prioul, R., 2014. Injection-Sensitive Mechanics of Hydraulic Fracture Interaction with Discontinuities. Rock Mechanics and Rock Engineering. 47, 1625–1640. https://doi.org/10.1007/s00603-014-0596-7

Cloutier, J., Kyser, K., Olivo, G.R., Alexandre, P., Halaburda, J., 2009. The Millennium Uranium Deposit, Athabasca Basin, Saskatchewan, Canada: An Atypical Basement-Hosted Unconformity-Related Uranium Deposit. Economic Geology. 104, 815–840. https://doi.org/10.2113/gsecongeo.104.6.815

Cox. S.F., Wall. V.J., Etheridgea. M.A., Potter, T.F., 1991. Deformational and metamorphic processes in the formation of mesothermal vein-hosted gold deposits - examples from the Lachlan Fold Belt in central Victoria, Australia. Ore Geology Reviews. 6, 391–423 https://doi.org/10.1016/0169-1368(91)90038-9

Cox, S.F., Knackstedt, M.A., Braun, J., 2001. Principles of structural control on permeability and fluid flow in hydrothermal systems. In: Richards JP, Tosdal RM (eds) Structural controls on ore genesis. Economic Geology, 14, 1–24. http://hdl.handle.net/1885/92810

Cox. S.F., Ruming, K., 2004. The St Ives mesothermal gold system, Western Australia—a case of golden aftershocks?. Journal of Structural Geology. 26, 1109–1125. https://doi.org/10.1016/j.jsg.2003.11.025

Cox, S.F., 2005. Coupling Between Deformation, Fluid Pressures, and Fluid Flow in Ore-producing Hydrothermal Systems at Depth in the Crust. United States, Society of Economic Geologists, Littleton, CO, USA, 100th Anniversary Volume, 39–75 https://doi.org/10.5382/AV100.04

Cui, T., Yang, J., Samson, I., 2012. Tectonic Deformation and Fluid Flow: Implications for the Formation of Unconformity-Related Uranium Deposits. Economic Geology. 107, 147–163. https://doi.org/10.2113/econgeo.107.1.147

Cuney, M., 2009. The extreme diversity of uranium deposits. Mineralium Deposita. 44, 3–9. https://doi.org/10.1007/s00126-008-0223-1

Dahlkamp, F.J., 1978. Geologic Appraisal of the Key Lake U-Ni Deposits, Northern Saskatchewan. Economic Geology. 73, 1430–1449. https://doi.org/10.2113/gsecongeo.73.8.1430

Dehghan, A., Goshtasbi, K., Ahangari, K., Jin, Y., Bahmani, A., 2016. 3D Numerical Modeling of the Propagation of Hydraulic Fracture at Its Intersection with Natural (Pre-existing) Fracture. Rock Mechanics and Rock Engineering. 50, 367–386. https://doi.org/10.1007/s00603-016-1097-7

Derode, B., Guglielmi, Y., De Barros, L., Cappa, F., 2015. Seismic responses to fluid pressure perturbations in a slipping fault. Geophysical Research Letters. 42, 3197–3203. https://doi:10.1002/2015GL063671

Derome D., Cuney M., Cathelineau M., Fabre C.,Jean Dubessy J., Bruneton P., Hubert A., 2003. A detailed fluid inclusion study in silicified breccias from the Kombolgie sandstones (Northern Territory, Australia): inferences for the genesis of middle-Proterozoic unconformity-type uranium deposits. Journal of Geochemical Exploration. 80, 259 – 275 https://doi:10.1016/S0375-6742(03)00194-8

Dou, F., Wang, J.G., Wang, H., Hu, B., Li, C., 2019. Discrete Element Analysis for Hydraulic Fracture Propagations in Laminated Reservoirs with Complex Initial Joint Properties. Geofluids. 1, 1–23. https://doi.org/10.1155/2019/3958583

Earle, S., Sopuck, V., 1989. Regional lithogeochemistry of the eastern part of the Athabasca Basin uranium province, Saskatchewan, in Muller-Kahle, E., ed., Uranium resources and geology of North America: International Atomic Energy Agency, TECDOC-500, p. 263–269.

Eldursi, K., Chi, G., Bethune, K., Li, Z. Ledru, P., Quirt, D., 2021a. New insights from 2- and 3-D numerical modelling on fluid flow mechanisms and geological factors responsible for the formation of the world-class Cigar Lake uranium deposit, eastern Athabasca Basin, Canada. Mineralium Deposita. 56, 1365–1388. https://doi.org/10.1007/s00126-020-00979-5

Eldursi, K., Scholtes, L., Conin, M., Golfier, F., Mercadier, J., Ledru, Collon, P., Chemillac, R., 2021b. Fault Reactivation Mechanisms: Insights From 3-D Hydromechanical Modeling of Unconformity-Related Uranium Deposits, Athabasca Basin, Northern Canada. AGU meeting, New Orleans, USA. https://ui.adsabs.harvard.edu/abs/2021AGUFMMR51A..07E/abstract

Emsbo, P., Seal, R., Breit, G., Diehl, S., Shah K., 2016. Sedimentary exhalative (sedex) zinc-lead-silver deposit model: U.S. Geological Survey Scientific Investigations Report 2010–5070–N, 57 p. https://doi.org/10.3133/sir20105070N

Fayek, M. Kyser, T.K., 1997. Characteristics of multiple fluid events and rare earth element mobility associated with the formation of unconformity-type uranium deposits in the Athabasca Basin, Canada. Canadian Mineralogist. 35, 627–658.

Ferrill, D.A., Smart K.J., Morris A.P., 2019. Fault failure modes, deformation mechanisms, dilation tendency, slip tendency, and conduits versus seals. Geological Society, London, Special Publications. 496, 75–98. https://doi.org/10.1144/SP496-2019-7

Ferrill, D.A., Smart K.J., Morris A.P., 2020. Resolved stress analysis, failure mode, and fault-controlled fluid conduits. Solid Earth. 11, 899–908. https://doi.org/10.5194/se-11-899-2020

Ford, A., Blenkinsop, T., MCLellan, J., 2009. Factors affecting fluid flow in strike-slip fault systems: coupled deformation and fluid flow modelling with application to the western Mount Isa Inlier, Australia. Geofluids. 9, 2–23. https://doi.org/10.1111/j.1468-8123.2008.00219.x

Graham, G., 2020. Preliminary Economic Assessment for the Tthe Heldeth Túé (J Zone) Deposit, Waterbury Lake Property, Northern Saskatchewan, Canada. Technical report, 303 p.

Guffey, S., Piercey, S., Ansdell, K., Kyser, K., Kotzer, T., Quirt, D., Zaluski, G. 2019. Geochemical footprint of the Millennium unconformity-type uranium deposit, Canada:

implications for vectoring new targets. Geochemistry. Exploration, Environment, Analysis. 19(4), 395–413.
https://doi.org/10.1144/geochem2018-036

Guglielmi, Y., Cappa, F., Amitrano, D., 2008. High-definition analysis of fluid-induced seismicity related to the mesoscale hydromechanical properties of a fault zone. Geophysical Research Letter, 35, L06306.
https://doi.org/10.1029/2007GL033087

Guglielmi, Y., Elsworth, D., Cappa, F., Henry, P., Gout, C., Dick, P., Durand, J., 2015. In situ observations on the coupling between hydraulic diffusivity and displacements during fault reactivation in shales: AGU publication, Journal of Geophysical Research. Solid Earth. 120, 7729–7748.
https://doi:10.1002/2015JB012158

Guo, J., Zhao, X., Zhu, H., Zhang, X., Pan, R., 2015. Numerical simulation of interaction of hydraulic fracture and natural fracture based on the cohesive zone finite element method. Journal of Natural Gas Science and Engineering. 25, 180–188. http://dx.doi.org/10.1016/j.jngse.2015.05.008

Harrison G. 2015. Regional physical properties of the East Athabasca Basin: Preliminary review of Lab analysis and downhole probing data. Internal report 14-CDN-15-13 Orano p.

Hillacre, S., 2018. Structural analysis, paragenesis, and geochronology of the arrow uranium deposit, western athabasca basin, saskatchewan, canada: implications for the development of the patterson lake corridor, Saskatoon, Canada, M.Sc. thesis, University of Saskatchewan, 163 p.

Hoeve, J., Sibbald, T.I.I., 1978. On the genesis of Rabbit Lake and other unconformity-type uranium deposits in northern Saskatchewan, Canada. Economic Geology. 73, 1450-1473.
https://doi.org/10.2113/gsecongeo.73.8.1450

Hoeve, J., Quirt, D., 1984. Mineralization and host rock alteration in relation to clay mineral diagenesis and evolution of the Middle-Proterozoic, Athabasca Basin, northern Saskatchewan, Canada. Saskatchewan Research Council, Technical Report 187, 187 p.

Hu, Y., Wang, Q., Zhao, J., Chen, S., Zhao, C., Fu, C., 2020. Three-dimensional complex fracture propagation simulation: Implications for rapid decline of production capacity. Energy Science & Engineering. 8(12), 4196–4211.
https://doi.org/10.1002/ese3.804

Huang, N., Jiang, Y., Lic, B., Liu, R., 2016. A numerical method for simulating fluid flow through 3-D fracture networks. Journal of Natural Gas Science and Engineering. 33, 1271–1281.
https://doi.org/10.1016/j.jngse.2016.06.072

Hubbert, M.K., Rubey, W.W., 1959. Role of fluid pressure in mechanics of overthrust faulting: I. mechanics of fluid-filled porous solids and its application to overthrust faulting. Geological Society of America Bulletin. 70, 115–166.
https://doi.org/10.1130/0016-7606(1959)70[115:ROFPIM]2.0.CO;2

Huston, D.L., Ayling, B.F., Connolly, D.P., Lewis, B., Mernagh, T.P., Schofield, A., Wielen, S.E., 2010. An assessment of the uranium and geothermal potential of north Queensland. Canberra, Geoscience Australia, 108 p. https://www.ga.gov.au/products/servlet/controller?event=GEOCAT_DETAILS&catno=69711

IAEA, 2018. Geological classification of uranium deposits and description of selected examples. IAEA-TECDOC-1857, 295 p.

Itasca, 2013. "3DEC Version 5.0, 3-Dimensional Distinct Element Code," User's Manual, Itasca Consulting Group Inc., Minneapolis, MN US.

Jaky, J., 1944. The coefficient of earth pressure at rest. Journal of the Society of Hungarian Architects and Engineering. 7, 355–358.

Jefferson, C., Thomas, D., Gandhi, S., Ramaekers, P., Delaney, G., Brisbin, D., Cutts, C., Portella, P., Olson, R., 2007. Unconformity associated uranium deposits of the Athabasca Basin, Saskatchewan and Alberta. In: EXTECH IV: Geology and Uranium Exploration Technology of the Proterozoic Athabasca Basin, Saskatchewan and Alberta: Geological Survey of Canada, Bulletin 588, (also Geological Association of Canada, Mineral Deposits Division, Special Publication 4; Saskatchewan Geological Society, Special Publication 18) Vol. 588 (eds Jefferson CW, Delaney G), Geological Survey of Canada, Ottawa, p. 23–67.

Jeanneret P., Goncalves, P., Durand, C., Trap, P., Marquer, D., Quirt, D., Ledru, P., 2016. Tectono-metamorphic evolution of the pre-Athabasca basement within the Wollaston-Mudjatik Transition Zone, Saskatchewan. Canadian Journal of Earth Sciences, 53, 231–259. https://doi.org/10.1139/cjes-2015-0136

Kakurina, M., Guglielmi, Y., Nussbaum, C., Valley B. 2019. Slip perturbation during fault reactivation by a fluid injection. Tectonophysics. 757, 140–152, https://doi.org/10.1016/j.tecto.2019.01.017

Kotzer, T., Kyser, T.K., 1995. Petrogenesis of the Proterozoic Athabasca Basin, northern Saskatchewan, Canada, and its relation to diagenesis, hydrothermal uranium mineralization and paleohydrogeology: Chemical Geology, v. 120, p. 45–89. https://doi.org/10.1016/0009-2541(94)00114-N

Kyser, K, Hiatt, E, Renac, C, Durocher, K, Holk, G, Deckart, K., 2000. Diagenetic fluids in paleo- and meso-proterozoic sedimentary basins and their implications for long protracted fluid histories. In: Kyser TK (ed) Fluids and basin evolution. Mineralogical Association of Canada Short Course. 28, 225–262.

Ledru, P., Benedicto, A., Poh, J., Robbins, J. 2019. "Implications of a new tectonic model on the role of pre-Athabasca basement-hosted fault systems in the formation of the unconformity related uranium deposits," in Open House Abstract Volume, Saskatchewan Ministry of Energy and Resources, p. 4, Saskatchewan Geological Survey.

Ledru, P., Benedicto, A., Chi, G., Khairallah, C., 2023. "The unconformity-related uranium mineral system of the Athabasca Basin (Canada)," in Dans Ressources métalliques 2, S. Decrée, Ed., ISTE Editions, London.

Leach, D., Bradley, D., Lewchuk, M., Symons, D., Marsily, G., Brannon, J., 2001. Mississippi Vally-Type Lead-Zinc deposits through geological time: implications from recent age-dating research. Mineralium Deposita. 36, 711–740. https://doi.org/10.1007/s001260100208

Li, Y., Hu, W., Zhang, Z., Zhang, Z., Shang, Y., Han, L., Wei, S., 2021. Numerical simulation of hydraulic fracturing process in a naturally fractured reservoir based on a discrete fracture network model. Journal of Structural Geology. 147, 1–12 https://doi.org/10.1016/j.jsg.2021.104331

Li, Z., Chi, G., Bethune, K., Eldursi, K., Quirt, H.D., Ledru, P., Gudmundson, G., 2018. Numerical simulation of strain localization and its relationship to formation of the Sue unconformity-related uranium deposits, eastern Athabasca Basin, Canada. Ore Geology Reviews. 101, 17–31. https://doi.org/10.1016/j.oregeorev.2018.07.004

Martz, P., Cathelineau, M., Mercadier, J., Boiron, M., Jaguin, J., Tarantola, A., Demacon, M., Gerbeaud, O., Quirt, D., Doney, A., Ledru, P., 2017. C-O-H-N fluids circulations and graphite precipitation in reactivated Hudsonian shear zones during basement uplift of the Wollaston-Mudjatik Transition Zone: example of the Cigar Lake U deposit. Lithos. 295, 222–245. https://doi.org/10.1016/j.lithos.2017.10.001

Martz, P., Mercadier, J., Cathelineau, M., Boiron, M., Quirt, D., Doney, A., Gerbeaud, O., De Wally, E., Ledru, P., 2019. Formation of U-rich mineralizing fluids through basinal brine migration within basement-hosted shear zones: a large-scale study of the fluid chemistry around the unconformity-related Cigar Lake U deposit (Saskatchewan, Canada). Chemical Geology. 508, 116–143. https://doi.org/10.1016/j.chemgeo.2018.05.042

Ma, X., Zhou, T., and Zou, Y., 2017. Experimental and numerical study of hydraulic fracture geometry in shale formations with complex geologic conditions. Journal of Structural Geology. 98, 53–66. https://doi.org/10.1016/j.jsg.2017.02.004

Mayne, P.W., Peuchen, J., Bouwmeester, D., 2010. Soil unit weight estimation from CPTs: 2nd International Symposium on Cone Penetration Testing, Huntington Beach, CA, USA, May 2010

Meixner, J., Schill, E., Grimmer, J.C., Gaucher, E., Kohl, T., Klingler, P., 2016. Structural control of geothermal reservoirs in extensional tectonic settings: An example from the Upper Rhine Graben. Journal of Structural Geology. 82, 1–15. https://doi.org/10.1016/j.jsg.2015.11.003

Muchez, P., Heijlen, W., Banks, D., Blundell, D., Boni, M., Grandia, F., 2005. Extensional tectonics and the timing and formation of basin-hosted deposits in Europe. Ore Geology Reviews, 27, 241–267. https://doi.org/10.1016/j.oregeorev.2005.07.013

Mwenifumbo, C.J., Elliott, B.E., Jefferson, C.W., Bernius, G. R., Pflug, K.A., 2002. Physical Rock Properties From the Athabasca Formations; Designing Geophysical Exploration Models for Uranium Deposits. Journal of Applied Geophysics.

Pagel, M., 1975. Détermination des conditions physico-chimiques de la silicification diagénétique des grès Athabasca (Canada) au moyen des inclusions fluids. Comptes Rendus Série D, 280, 2301–2304.

Pascal, C., 2002. Interaction of faults and perturbation of slip: influence of anisotropic stress states in the presence of fault friction and comparison between Wallace–Bott and 3D Distinct Element models. Tectonophysics. 356(4), 307–322. https://doi.org/10.1016/S0040-1951(02)00413-4

Peacock, D., Nixon, C., Rotevatn, A., Sanderson, D., Zuluaga, L., 2017. Interacting faults. Journal of Structural Geology. 97, 1–22. https://doi.org/10.1016/j.jsg.2017.02.008

Perkins, T., Normore, N., Hamel, C., 2017. The christie lake project, saskatchewan. Technical report prepared for UEX Corporation. Report for NI 43-101, 131 p. https://www.uexcorp.com/_resources/reports/Christie-Lake-Report-2016.pdf

Person, M., Hofstra, A., Sweetkind, D., Stone, W., Cohen, D., 2012. Analytical and numerical models of hydrothermal fluid flow at fault intersections. Geofluids. 12, 312–326. https://doi.org/10.1111/gfl.12002

Pochon, A., Gloaguen, E., Branquet, Y., Poujol, M., Ruffet, G., Boiron, M., Boulvais, P., Gumiaux, C., Cagnard, F., Gouazou, F., Gapais, D., 2018. Variscan Sb-Au mineralization in Central Brittany (France): A new metallogenic model derived from the Le Semnon district. Ore Geology Reviews. 97, 109–142. https://doi.org/10.1016/j.oregeorev.2018.04.016

Poh, J., Yamato, P., Duretz, T., Gapais, D., Ledru, P., 2020 “Pre-cambrian deformation belts in compressive tectonic regimes: a numerical perspective,” Tectonophysics, vol. 777, article 228350. https://doi.org/10.1016/j.tecto.2020.228350

Poh, J., Eldursi, K., Ledru, P., Yamato P., Benedicto, A., Chi, G., 2022. Role of Hydrothermal Circulation along and above Inherited Basement Structures Relating to Unconformity-Related Uranium Mineralization. Geofluids, Volume 2022, Article ID 9131289, 20 p. https://doi.org/10.1155/2022/9131289

Polito, P., Kyser, K., Marlatt, J., Alexandre, P., Bajwah, Z., Drever, G., 2004. Significance of the alteration assemblages for the origin and evolution of the Proterozoic Nabarlek unconformity-related uranium deposit, Northern Territory, Australia. Economic Geology. 99, 113–139. https://doi.org/10.2113/gsecongeo.99.1.113

Power, M.J., Hattori, K., Sorba, C., Potter, E.G., 2012. Geochemical anomalies in soils and uppermost siliciclastic units overlying the Phoenix uranium deposit, Athabasca Basin,

Saskatchewan. Geological Survey of Canada, Open File 7257, p. 37 https://doi.org/10.4095/291981

Quirt, D.H. 2003. Athabasca unconformity-type uranium deposits: One deposit type with many variations. *In*: Uranium Geochemistry (Cuney, M., ed.), International Conference Proceedings, Géochime de l'Uranium 2003, Université Henri-Poincaré (Nancy, France), 309–312.

Rempe, M., Di Toro, G., Mitchell, T.M., Smith, S.A.F., Hirose, T., Renner, J., 2020. Influence of effective stress and pore fluid pressure on fault strength and slip localization in carbonate slip zones. Journal of Geophysical Research: Solid Earth, 125, e2020JB019805. https://doi.org/10.1029/2020JB019805

Rhys, D., Eriks, S., Horn, L., 2010. A new look at basement hosted new look at basement-hosted mineralization in the Horseshoe and Raven deposits, eastern Athabasca Basin [abs.]: Open House Meeting, Saskatoon, Canada, 2010, abstract, p. 91.

Ruhl, C. J., Abercrombie, R. E., Smith, K. D., and Zaliapin I., 2016, Complex spatiotemporal evolution of the 2008 Mw 4.9 Mogul earthquake swarm (Reno, Nevada): Interplay of fluid and faulting. Journal of Geophysical Research Solid Earth. 121, 8196–8216 https://doi.org/10.1002/2016JB013399

Rutqvist, J., 2015. Fractured rock stress-permeability relationships from in situ data and effects of temperature and chemical-mechanical couplings. Geofluids. 15, 48–66. https://doi.org/10.1111/gfl.12089

Schofield, M., 2016. Geochemical footprints and structural localisation of ore-grade Au mineralisation: insights from the Karangahake deposit, New Zealand. M.S. Thesis University of Auckland, p. 101

Shelly, D. R., Taira, T., Prejean, S. G., Hill, D. P., Dreger, D. S., 2014. Fluid-faulting interactions: Fracture-mesh and fault-valve behavior in the February 2014 Mammoth Mountain, California, earthquake swarm. Geophysical Research Letters. 42, 5803–8512 https://doi.org/10.1002/2015GL064325

Shepherd, T., Bouch, J., Gunn, A., McKerve,y J., Naden, J., Scrivener, R., Styles, M., Large, D., 2005. Permo–Triassic unconformity-related Au-Pd mineralisation, South Devon, UK: new insights and the European perspective. Mineralium Deposita. 40, 24–44. https://doi.org/10.1007/s00126-004-0459-3

Shiu, W., Guglielmi, Y., Graupner, B., Rutqvist, J. 2021. Modelling the water injection induced fault slip and its application to in-situ stress estimation. International Journal of Rock Mechanics and Mining Sciences. 137, 104537. https://doi.org/10.1016/j.ijrmms.2020.104537.

Sibson, R., 1977. Fault rocks and fault mechanisms. Journal of the Geological Society. 133 (3), 191–213. http://dx.doi.org/10.1144/gsjgs.133.3.0191

Sibson R.H., Robert F., and Howard K., 1988. High-angle reverse faults, fluid-pressure cycling, and mesothermal gold-quartz deposits. Geology. 16, 551–555.

https://doi.org/10.1130/0091-7613(1988)016<0551:HARFFP>2.3.CO;2

Sibson, R., 1995. Selective fault reactivation during basin inversion: potential for fluid redistribution through fault-valve action. From BUCHANAN, J. G. & BUCHANAN, P. G. (eds), 1995, Basin Inversion, Geological Society Special Publication No. 88, 3–19. https://doi.org/10.1144/GSL.SP.1995.088.01.02

Sibson, R., 2001. Seismogenic Framework for Hydrothermal Transport and Ore Deposition. The Society of economic geologists, Book Chapter, Structural Controls on Ore Genesis, 25–48. https://doi.org/10.5382/Rev.14.02

Sibson, R. H., 2020. Preparation zones for large crustal earthquakes consequent on fault-valve action. Earth, Planets and Space. 72:31 1–20. https://doi.org/10.1186/s40623-020-01153-x

Terzaghi, K., 1923. Die Berechnung der Durchlassigkeitszilfer des tones aus dem Verlauf der Hydrodynamischen Spannungserscheinungen (Calculation of the Porosity Index of Clay from Hydrodynamic Tension Conditions). Akademie der Wissenschaften, Vienna, v. 132 (3–4), p. 125–128.

Tremblay, L.P., 1982. Geology of the uranium deposits related to the sub-Athabasca unconformity, Saskatchewan. Technical report, GS-CAN-PAPER 81-20, 61 p.

Thomas, D., Aubin, A., Zaluski, G., 2016. What Does an Athabasca Basin Uranium Deposit Footprint Look Like? Empirical characteristics and the relevance to exploration. Oral presentation, Saskatchewan Geological Society Luncheon, Nov. 2016

Vidale, J. E., Shearer, P. M., 2006. A survey of 71 earthquake bursts across southern California: Exploring the role of pore fluid pressure fluctuations and aseismic slip as drivers. Journal Geophysical Research Solid Earth. 111, B05312. https://doi.org/10.1029/2005JB004034

Wallis, R.H., Saracoglu, N., Brummer, J.J., Golightly, J.P., 1985. Geology of the McClean uranium deposits. *In*: Geology of Uranium Deposits (Sibbald, T.I. and Petruk, W., eds.), Canadian Institute of Mining and Metallurgy, 32, 101–131.

Walsh, J.B., 1981. Effect of Pore Pressure and Confining Pressure on Fracture Permeability. International Journal of Rock Mechanics and Mining Sciences & Geomechanics Abstracts. 18, 429-435. https://doi.org/10.1016/0148-9062(81)90006-1

Wilkinson, J., 2014. Sediment-Hosted Zinc–Lead Mineralization. In: Holland H. and Turekian K. (eds.) Treatise on Geochemistry, Second Edition, 13:219–249Yang J., Large R., Bull S. (2004) Factors controlling free thermal convection in faults in sedimentary basins: implications for the formation of zinc-lead mineral deposits: Geofluids, v. 4, p. 237–247. https://doi.org/10.1016/B978-0-08-095975-7.01109-8

Wilson, M.R. Kyser, T.K., 1987. Stable isotope geochemistry of alteration associated with the Key Lake uranium deposit. Economic Geology.82, 1450–1557.

Witherspoon, P.A., Wang, J. S.Y., Iwai, K., Gale, J.E., 1980. Validity of Cubic Law for fluid flow in a deformable rock fracture. Water Resources Research. 16, 1016–1024. https://doi.org/10.1029/WR016i006p01016

Yin, Z., Huang, H., Zhang, F., Zhang, L., Maxwell, S., 2020. Three-dimensional distinct element modeling of fault reactivation and induced seismicity due to hydraulic fracturing injection and backflow. Journal of Rock Mechanics and Geotechnical Engineering. 12, (4), 752–767. https://doi.org/10.1016/j.jrmge.2019.12.009.

Zhang, Q., Zhang, X., Sun, W., 2020. Hydraulic fracturing in transversely isotropic tight sandstone reservoirs: A numerical study based on bonded-particle model approach. Journal of Structural Geology. 136, 1–13. https://doi.org/10.1016/j.jsg.2020.104068

Zhou, J., Chen, M., Jin, Y., Zhang, G., 2008. Analysis of fracture propagation behavior and fracture geometry using a tri-axial fracturing system in naturally fractured reservoirs. International Journal of Rock Mechanics and Mining Sciences. 7, 1143–1152. https://doi.org/10.1016/j.ijrmms.2008.01.001

Zou, Y., Zhang, S., Ma, X., Zhou, T., and Zeng, B., 2016, Numerical investigation of hydraulic fracture network propagation in naturally fractured shale formations. Journal of Structural Geology. 84, 1–13. https://dx.doi.org/10.1016/j.jsg.2016.01.004